A Bayesian CAIPIVAT Approach with Through-Plane Acceleration to Enhance Efficiency of Simultaneously Encoded Slice Acquisition in FMRI

Ke Xu[a], Daniel B. Rowe[a,*]

[a] *Computational Mathematical and Statistical Sciences, Marquette University, 1313 W Wisconsin Ave, Milwaukee, 53233, WI, USA*

Abstract

FMRI has been a safe medical imaging tool to study brain function by demonstrating the spatial and temporal changes in brain metabolism in recent decades. To capture brain functionality more efficiently, efforts have been made to accelerate the number of images acquired per unit of time that create each volume image without losing full anatomical structure. The Simultaneous Multi-Slice (SMS) technique provides a reconstruction method where multiple slices are acquired and aliased concurrently. Traditional imaging techniques such as SENSE and GRAPPA can reconstruct an image from less measured data but have their drawbacks. The Controlled Aliasing in Parallel Imaging (CAIPI) and view angle tilting (VAT) techniques achieve slice-wise image shift to decrease the influence of the geometry factor (g-factor) of coil sensitivities and prevent the singular problem of the design matrix. In this paper, a Bayesian CAIPIVAT approach for multi-coil separation of parallel encoded complex-valued slices (mSPECS-CAIPIVAT) with a novel SMS approach is presented and combined with the Hadamard phase-encoding method for image separation. Our proposed approach was applied to simulation and experimental studies showing a decrease in the influence of the g-factor while increasing the brain activation detection rate. The signal-to-noise ratio and the contrast-to-noise ratio are also improved by our approach.

Keywords:

*Corresponding author.
Email address: daniel.rowe@marquette.edu (Daniel B. Rowe)

1. Introduction

As a powerful and non-invasive medical imaging tool, functional Magnetic Resonance Imaging (fMRI) has played a dominant role in brain imaging studies since 1990 ([18]). The activity of neurons cannot be directly detected but is correlated to the Blood Oxygen Level Dependence (BOLD) contrast signal which is used as a proxy. By detecting task-related changes in the BOLD signal inside our brain, the magnetic resonance (MR) scanner can map our brain with a unique radio frequency (RF) pulse sequence ([18]; [4]). The Gradient Echo Echo-Planer Imaging (GE-EPI) pulse sequence is widely used in fMRI studies to shorten the scan time and decrease the influence of the motion of subjects by acquiring full k-space spatial information within a single excitation ([14]; [22]; [19]). In structural and functional MRI studies, the time to measure a volume image is dependent upon how rapidly the amount of data necessary to reconstruct an image can be measured. In order to accelerate the number of images measured per unit time, a topic of study has been to measure less data but still be able to reconstruct a high-quality image. To reconstruct images using less data, multiple receiver coils are used where each coil measures sensitivity-weighted images ([6]). Initially, accelerated imaging was aimed at In-Plane Acceleration (IPA) where spatial frequency data are partially skipped, and each coil measured fewer lines of the spatial frequency array. In parallel imaging techniques, like Sensitivity Encoding (SENSE) and Generalized Autocalibrating Partially Parallel Acquisitions (GRAPPA) ([21]; [5]), a single slice has been excited, and partial lines of k-space skipped, resulting in a sensitivity weighted aliased image for each coil, that is combined into a single complete image. Bayesian techniques have been applied to improve the resolution of the reconstructed images by incorporating the anatomical information from prior distributions into the k-space ([12]; [11]). Other in-plane imaging acceleration techniques like partial Fourier imaging technique ([3]; [17]) can acquire half of the lines in the k-space. The unacquired spatial frequency data can be determined due to the Hermitian symmetry property of the k-space to reconstruct real-valued images. Moreover, a rapid three dimensional volume-image method has been established to sample the k-space ([13]). However, considering some fixed time blocks in the data-acquiring process, for instance, imaging encoding

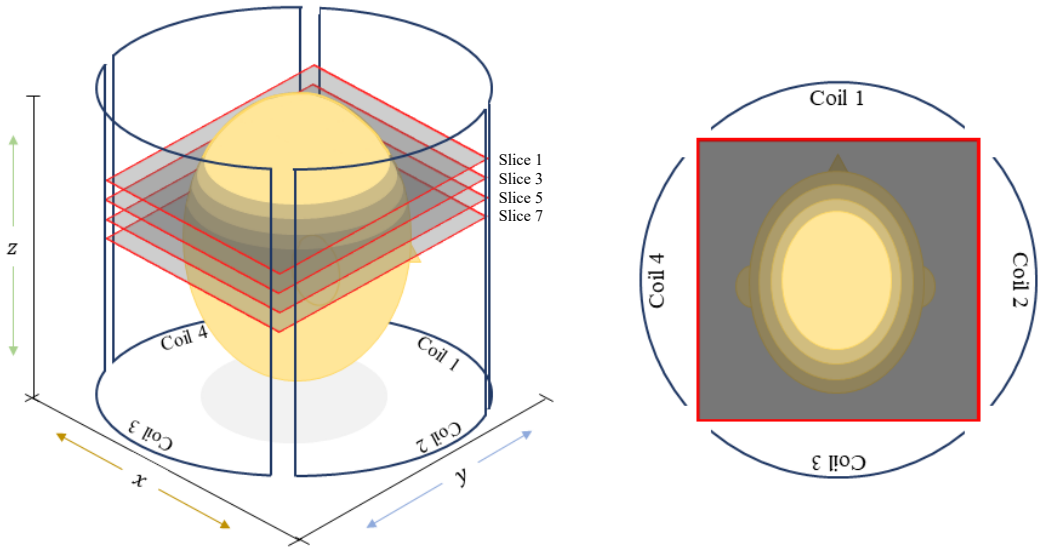

Figure 1: The 3D view (left) and 2D view (right) of an example for SMS technique with four slices and four coils.

and the proper time for T_2^* contrast in one excitation, the scan time will not decrease significantly in IPA techniques. More recently, Simultaneous Multi-Slice (SMS) techniques (Fig. 1) were developed and discussed ([28]; [26]; [1]). The SMS technique is extensively used in fMRI studies, and it allows for acquiring fMRI data with high resolution by using a multiband (MB) radiofrequency (RF) within a reduced repetition time (TR). Compared with conventional parallel imaging techniques, in SMS techniques, multiple slices are acquired concurrently and aliased together in one excitation, and hence, the image-acquiring time will decrease with a factor of the total number of aliased slices. Thus, a Through-Plane Acceleration (TPA) is achieved by SMS techniques and allows for a more efficient approach to acquiring images. In this paper, a novel SMS imaging reconstruction technique with high acceleration factor, a Bayesian Controlled Aliasing in Parallel Imaging with View Angle Tilting approach for multi-coil Separation of Parallel Encoded Complex-valued Slices (mSPECS-CAIPIVAT), is presented and discussed.

Since multiple slices are acquired at the same time for one excitation of the TPA technique, a short distance between aliased slices will lead to a high similarity of voxel and coil sensitivity information. When applying the standard SENSE method, this may cause a singular matrix problem and

strong inter-slice signal leakage will appear on the reconstructed images. To decrease the influence of the geometry properties of the coil sensitivity maps, techniques like "controlled aliasing in parallel imaging results in higher acceleration" (CAIPIRINHA), "blipped-CAIPIRINHA" (Blipped-CAIPI), and Hadamard phase-encoding provide other possible ways to minimize the influence of the geometric factor (g-factor) and increase the conditioning of the slices aliasing matrix ([2]; [27]). By modulating the phase for each line in k-space and imparting each line with a specific angle, the field-of-view (FOV) is moved in the phase encoding direction (PE, vertically in this paper). Applying a unique phase modulation amount to each slice in the aliased image-acquiring process increases the physical distance between the aliased voxels. Therefore, the difference of coil sensitivity for each slice will increase and the influence of the g-factor for each excitation is minimized. Moreover, to further increase the physical distance between two aliased voxels and expose more information beneath the coil sensitivities, the FOV can not only be moved along the vertical PE direction but also the horizontal readout direction (RO, horizontally in this paper). The study "multislice CAPIPRINHA using view angle tilting technique" (CAIPIVAT) ([7]; [8]) proposes a method combining the CAIPIRINHA technique and View Angle Tilting (VAT) ([9]) technique together by applying a unique compensation gradient of VAT. Other techniques to solve the singular matrix problem of the design matrix, like the "simultaneous multi-slice acquisition" (SIMA) ([28]) method discussed a powerful tool, the Hadamard phased-encoding technique in the reconstruction process. By incorporating a specific coefficient from the Hadamard matrix for each aliasing slice, different combinations for each voxel is achieved. For example, the summation of two desired voxels will not only be acquired but also the difference between two voxels is collected. Moreover, the Hadamard phase-encoding technique has been proved to be a significant method to minimize the residual correlation between the unaliased images and improve the temporal signal-to-noise ratio ($tSNR$) ([15]; [16]). In the "Separation of parallel encoded complex-valued slices (SPECS) from a single complex-valued aliased coil image" and "multi-coil separation of parallel encoded complex-valued slices" (mSPECS) studies, the Hadamard phase encoding technique is also the essential idea ([24]; [10]). The SPECS technique and the mSPECS technique are critical milestones of this study.

In our mSPECS-CAIPIVAT model, we incorporate slice-wise image shift techniques and the Hadamard phase-encoding technique together in which different voxel combinations is acquired for each excitation. In the unaliasing

process, calibration reference images are artificially aliased, and the artificial aliasing matrix used to assess hyperparameters of prior distributions in the separation process. The artificial aliased calibration imaging technique and bootstrap sampling approach is combined and applied into the model to eliminate inter-slice signal leakage in the reconstruction images at the cost of a slightly increased variance of the calibration images forming the prior variance. The maximum *a posteriori* technique is applied in this model to calculate the estimated reconstruction voxel values. The mSPECS-CAIPIVAT model provides a solution to significantly reduce the scan time with a high acceleration factor, meanwhile providing high-resolution and high-quality reconstruction images.

2. Theory

2.1. The Data Acquiring Process

2.1.1. CAIPIRINHA and CAIPIVAT

As mentioned in Section. 1, the physical distance between two aliased voxels can be increased by applying the VAT, the CAIPIRINHA and the CAIPIVAT techniques to achieve slice-wise image shifts, thus reducing the dependence on the geometry of the coil array. The CAIPIRINHA technique can move the FOV along the PE direction (vertical) by modulating the phase for each line in k-space. Whereas the CAIPIVAT technique can shift the FOV along two directions, PE (vertical) and RO (horizontal), by applying a unique compensation gradient of VAT. Through these two image shift techniques along with the Hadamard slice encoding technique, the g-factor of the reconstructed images can be reduced. Since the g-factor is related to the signal-to-noise ratio (SNR), in SMS studies, giving the definition of the SNR:

$$SNR_{SMS} = SNR_{full}/(g\sqrt{R}), \tag{1}$$

where R is the IPA factor. From Eq. 1, the SNR_{SMS} is strongly influenced by the geometric properties of the coil array, g-factor. It depends on the number and location of the coils, the phase-encoding direction, the voxel location, etc. Thus, the g-factor is not a constant value but varies across each voxel within the images ([20]). A short physical distance between two aliased voxels will increase the g-factor value because of their intensity and sensitivity similarity which will decrease the SNR. Therefore, increasing the physical distance between two aliased voxels is one of our strategies. The

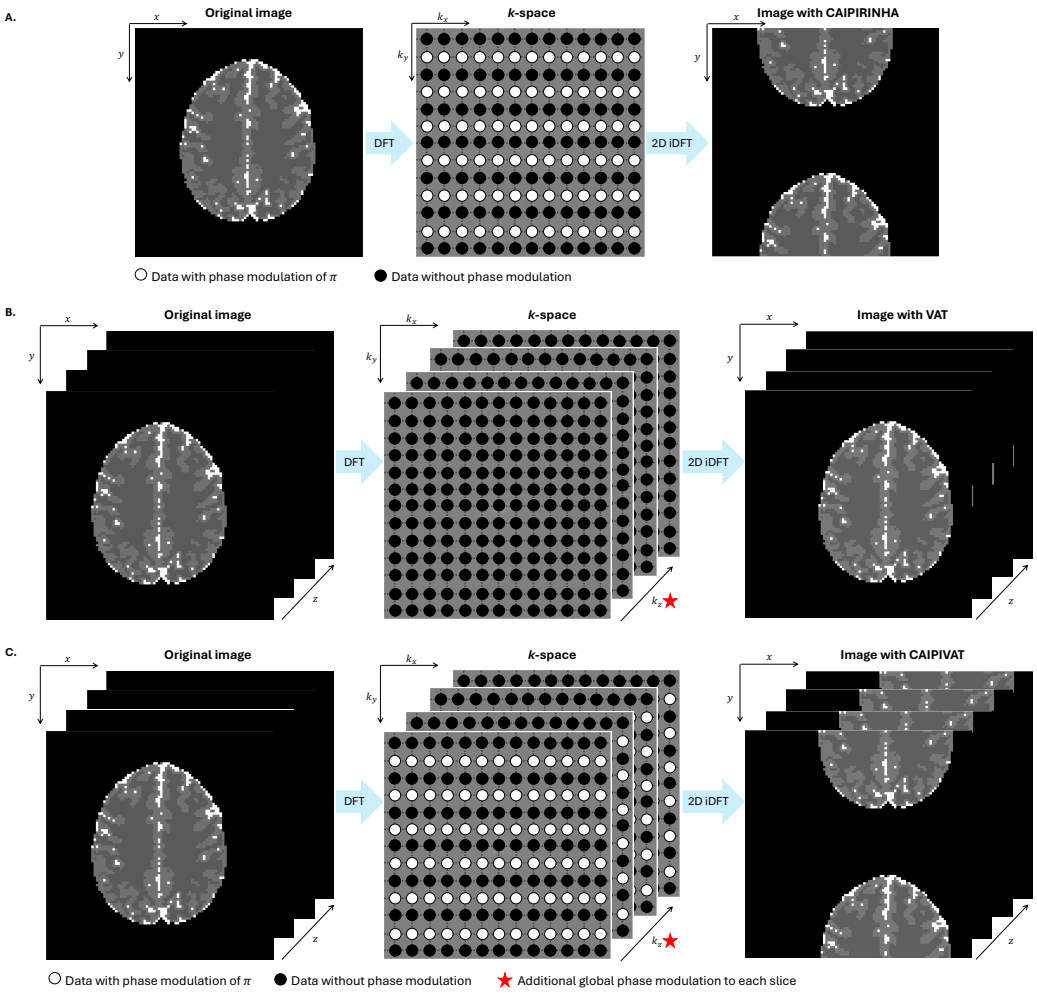

Figure 2: A. An illustration of the CAIPIRINHA process. B. An illustration of the VAT process. C. An illustration of the CAIPIVAT process.

VAT technique, the CAIPIRINHA technique, and the CAIPIVAT technique can reduce the influence of the g-factor by applying a partial in-plane image shift. Considering the 1D inverse discrete Fourier transform, a periodic time series $y(t)$ sampled at n time points Δt apart is described as below:

$$y(p\Delta t) = \sum_{q=-\frac{n}{2}}^{\frac{n}{2}-1} f(q\Delta\nu) e^{i\frac{2\pi}{n}pq}, \tag{2}$$

where $\Delta\nu$ is the temporal frequency resolution and $\Delta\nu = 1/(n\Delta t)$. It is the summation of the Fourier amplitude coefficients at multiple various frequencies. In Eq. 2, $y(p\Delta t)$ and $f(q\Delta\nu)$ are complex-valued quantities with real and imaginary components. When we shift the whole time series from $p\Delta t$ to $p'\Delta t$, where $y(p'\Delta t)$ is same as $y(p\Delta t)$ sampled at n time points Δt apart with a different order from $y(p\Delta t)$, a field-of-view shift Δy occurs and is:

$$\Delta y = y((p-p')\Delta t) = \sum_{q=-\frac{n}{2}}^{\frac{n}{2}-1} f(q\Delta\nu) e^{i\frac{2\pi}{n}pq} e^{-i\frac{2\pi}{n}p'q}, \tag{3}$$

for $p = 1, \ldots, n$. The FOV shift only depends on the phase change in k-space, which equals $-2\pi p'q/n$. If $p' = 1$, which means the image moves one voxel distance in the PE direction, the modulation quantity of phase is $-2\pi q/n$. If half of the image is shifted in the PE direction (FOV/2), $p' = n/2$, the modulation of phase should be $-\pi q$. Therefore, the phase of even lines in k-space should impart π and the phase of odd lines should impart 0. If the FOV/4 shift of the image needs to be achieved, the modulation of the phase for each line in the k-space needs to be adjusted. Fig. 2A is an illustration to explain the CAIPIRINHA process. Applying the discrete Fourier transform to each excitation in the time series to obtain the k-space, modulating the phase for each line in the k-space with a unique angle, after the inverse discrete Fourier transform, we will have an in-plane image shifted effect. Compared with the on-resonance spins of the CAIPIRINHA technique, during the slice-selection process, the CAIPIVAT technique allows off-resonance spins at different locations. Fig. 2B is an illustration to explain the VAT process. The VAT technique projects the excited spins along a unique view angle to map the brain with a specific spatial shift on the image plane. Fig. 2C is an illustration to explain the CAIPIVAT process. After the Fourier transform to acquire the k-space of the original image, the CAIPIRINHA technique is applied to the k-space of each slice. A global phase modulation is added to each slice at the same time.

In this paper, the principal idea of the CAIPIRINHA technique is applied first. For each slice within each excitation, we imply $\Delta y = (l-1)FOV/N_s$ in-plane image shift, where $l = 1, \ldots, N_s$ and N_s is the total number of aliased slices. On the TR dimension, we also imply the CAIPIRINHA technique for each excitation by $\Delta y = (m-1)FOV/N_s$ in-plane image shift, where $m = 1, \ldots, N_s$. Thus, with the in- and through-excitation image shift, at the $TR = N_s + 1$ excitation time point, the aliased artifacts should be the same as the $TR = 1$ excitation time point. Fig. 3A shows an example of an in-

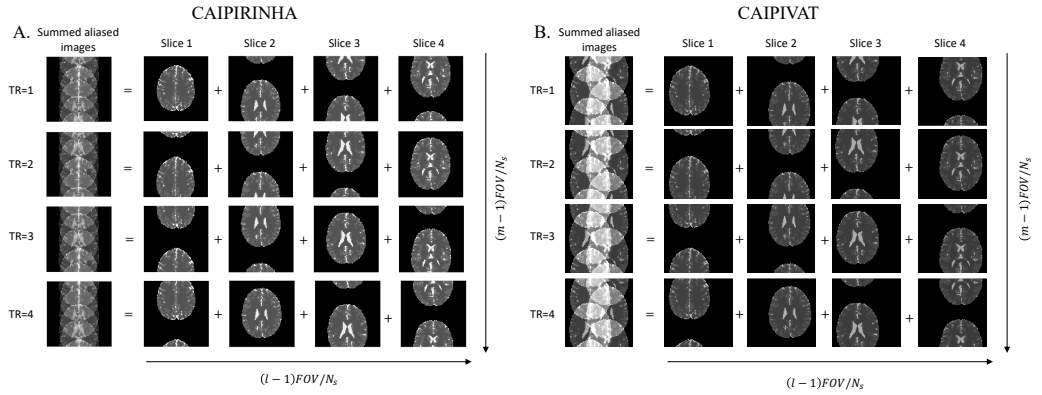

Figure 3: A. An example of in- and through-excitation image shift process with $N_s = 4$ by applying the CAIPIRINHA technique. B. An example of in- and through-excitation image shift process with $N_s = 4$ by applying the CAIPIVAT technique.

and through-excitation image shift process with $N_s = 4$ incorporating with the CAIPIRINHA technique. When $TR = 5$, the image shift pattern for each slice should be the same as the time point $TR = 1$. Furthermore, the principal idea of the CAIPIVAT technique will also be applied. Similar to the CAIPIRINHA technique, $\Delta y = (l-1)FOV/N_s$ for the in-plane image shift and $\Delta y = (m-1)FOV/N_s$ for the through-plane image shift is applied to each excitation along the PE direction. For each slice within each excitation, a unique image shift will appear horizontally on the RO direction with the support of the CAIPIVAT technique. The shift distance for each slice along the RO direction can be calculated and depends on the distance between the desired aliased slices, the compensation gradient, and the RO gradient. A modest slice-wise shift is applied for each excitation to ensure the brain image is not outside the FOV. Fig. 3B displays an example of in- and through-excitation image shift process of $N_s = 4$ incorporating with the CAIPIVAT technique. Besides the same amount of the FOV shift in- and through-excitation on the PE direction as CAIPIRINHA technique, slice 1 and slice 3 will have a FOV shift to the left and slice 2 and slice 4 will have a FOV shift to the right on the RO direction according to the CAIPIVAT technique. Thus, comparing with the CAIPIRINHA technique approach, the overlapping area between two desired aliased images will decrease and the independence of the sensitivity for each coil will increase.

2.1.2. The Hadamard Phase Encoding

The Hadamard encoding technique is a well-developed volume excitation method. The conventional MR imaging techniques have been limited by the size of the matrix for the acquired aliased images. The Hadamard phase-encoding method allows the increment of the size of the acquired aliased image matrix by aliasing in both frequency and phase encoding dimensions. With the support of this simultaneous binary-encoded technique, the TR will decrease, and the *SNR* ratio will improve. The Hadamard matrix is given by:

$$H_{2^n} = \begin{bmatrix} H_{2^{n-1}} & H_{2^{n-1}} \\ H_{2^{n-1}} & -H_{2^{n-1}} \end{bmatrix} = H_2 \otimes H_{2^{n-1}}, \text{and } H_1 = \begin{bmatrix} 1 \end{bmatrix}, H_2 = \begin{bmatrix} 1 & 1 \\ 1 & -1 \end{bmatrix}, \quad (4)$$

where $\otimes$ denotes the Kronecker product. It is an orthogonal and full rank matrix with elements of either +1 or -1. In the mSPECS-CAIPIVAT study, each excitation is sequentially coordinated with a unique Hadamard aliasing pattern. To improve the computational efficiency, we select the size of the Hadamard phase-encoding matrix to be the same as the number of the aliased slices. Thus, the size of the Hadamard phase-encoding matrix is $N_s \times N_s$. In this aim, $H_{\delta,z}$ is the δth row and zth column element of Hadamard matrix corresponding to zth slice in δth TR. Same as the sequential properties of image shifts, the Hadamard phase-encoding aliasing pattern will cycle through along the TR dimension. For example, the Hadamard aliasing pattern of $TR = N_s + 1$ should be the same as $TR = 1$. Fig. 4 shows an example of the Hadamard aliasing pattern when $N_s = 4$. Fig. 4A shows a 4×4 Hadamard matrix, Fig. 4B shows the Hadamard coefficients for each slice in the fMRI time series, Fig. 4C shows the phantom brain images multiplied by Hadamard aliasing coefficients at the first 4 TRs. In order to increase the distance between two aliased voxels and reduce the influence of the g-factor, we introduce the term "packet" to indicate the slice aliasing circumstance. For example, under a circumstance with $N_s = 8$ and $N_\alpha = 2$, we put odd number slices into one packet (i.e., slice 1, slice 3, slice 5, and slice 7), and even number slices into another packet (i.e., slice 2, slice 4, slice 6, and slice 8). For each excitation, all slices in one packet are measured simultaneously as one single array. Therefore, we will have 2 packets in this situation, and both packets will coordinate with the same Hadamard phase-encoding aliasing pattern. With the help of the packet technique, the slice-to-slice signal leakage artifacts will diminish.

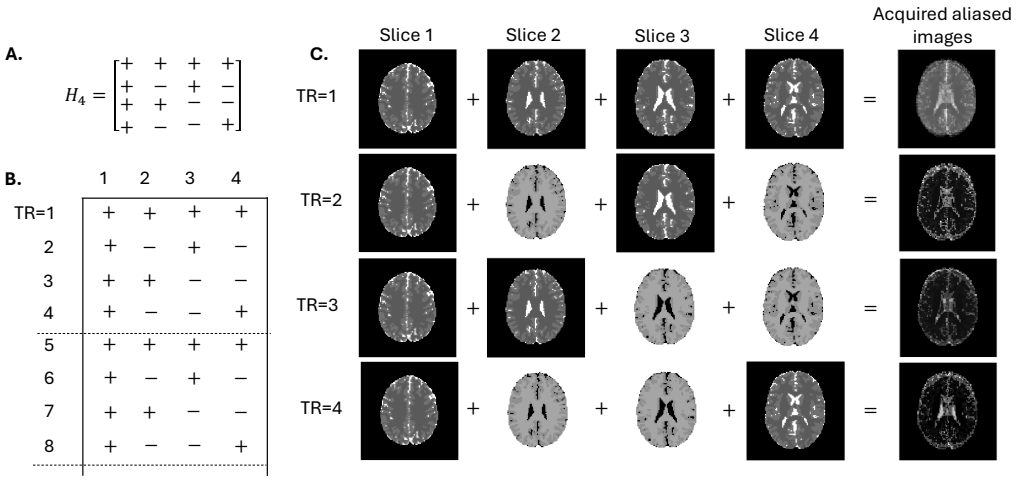

Figure 4: An illustration of Hadamard phase-encoding aliasing pattern when $N_s = 4$. A. shows the H_4 matrix with plus sign denotes as 1 and minus sign demotes as -1. B. shows sequential Hadamard aliasing coefficient for each slice in the fMRI time series. C. shows the phantom brain images are multiplied by the Hadamard aliasing coefficients at the first 4 TRs.

2.1.3. A Single Aliased Voxel

Given a single aliased voxel, $a_{j,\gamma,\delta}$, at the location (x, y) of aliased images, with δth Hadamard aliasing pattern and γth matrix rotation operation, measured at coil j, is defined as the summation equation:

$$a_{j,\gamma,\delta} = \sum\nolimits_{z=1}^{N_s} H_{\delta,z} R_{\gamma,z} S_{j,z} \beta_z + \varepsilon_j. \tag{5}$$

In Eq. 5, $a_{j,\gamma,\delta}$ is a 2×1 complex-valued vector with the real and imaginary components of the acquired aliased voxel value measured at coil j, with rotating operation γ and Hadamard phase-encoding aliasing pattern δ. The Hadamard phase-encoding aliasing pattern, $H_{\delta,z}$, is the same as the definition in Section 2.1.2, where parameter δ corresponds to the order of Hadamard coefficients pattern, and parameter z corresponds to the slice number. The coefficients of $H_{\delta,z}$ is either $+1$ or -1. The matrix rotation operator, $R_{\gamma,z}$, is closely related to the definition of Section 2.1.1. Subscript γ denotes the order of the matrix rotation operation for each TR, and parameter z corresponds to the number of slices. The coil sensitivity matrix, $S_{j,z}$, is a 2×2 skew symmetric matrix with the real and imaginary components at coil j for slice z, $S_(j, z) = [S_R, -S_I; S_I, S_R]_{j,z}$. The true voxel value, $\beta_z = [\beta_{zR}; \beta_{zI}]$, is a 2×1

vector with the real and imaginary parts of the aliased voxel in slice z, and the real part is stacked on the top of the imaginary part. The measurement noise, $\varepsilon_j = [\varepsilon_R; \varepsilon_I]$, is a 2×1 vector with real and imaginary parts stacked. The mean of measurement noise is $E(\varepsilon_j) = 0$, and the covariance of error is $cov(\varepsilon_j) = \sigma^2 I_2$, where I_2 is a 2×2 identity matrix.

Considering the measured aliased voxel in Eq. 5 across the N_c coils for N_s aliased slices with N_α time-points in the fMRI time series, Eq. 5 can be expressed as:

$$a = X_A \beta + \varepsilon. \tag{6}$$

N_α denotes the number of sequential time-points of the Hadamard encoded pattern, and it is an integer between 1 and N_s. Therefore, the net acceleration of the fMRI time series acquisition is defined as $A = N_s/N_\alpha$. In Eq. 6, the dimension of a is $2N_cN_\alpha \times 1$ including the real and imaginary components. The measurement error, ε, has the same dimension as a with the mean $E(\varepsilon) = 0$ and covariance $cov(\varepsilon) = \sigma^2 I_{2N_cN_\alpha}$. The dimension of the aliasing matrix, X_A, is $2N_cN_\alpha \times 2N_sN_r$, where N_r is an indicator of the number of matrix rotation operations. In this study, we generally assign $N_r = N_s$ to improve the computational efficiency. The true voxel value, β, has the dimension of $2N_sN_r \times 1$, including the real and imaginary value for each voxel. For the δth Hadamard aliasing pattern and γth matrix rotating operation, the aliasing matrix $(X_A)_{\gamma,\delta}$ across N_c coils is defined as:

$$(X_A)_{\gamma,\delta} = \left[H_{\delta,1} R_{\gamma,1} \left(\ S_{1,1}; \ldots ; S_{N_c,1} \ \right), \ldots, H_{\delta,N_c} R_{\gamma,N_c} \left(\ S_{1,N_s}; \ldots ; S_{N_c,N_s} \ \right) \right]. \tag{7}$$

$R_{\gamma,z}$ is the image shift indicator which operates on coil sensitivity maps for each slice, and not matrix multiplication. Across the N_α excitations, the aliasing matrix X_A is written as:

$$X_A = \left[(X_A)_1, \ldots, (X_A)_{N_\alpha} \right]'. \tag{8}$$

Since the measurement error has a Gaussian distribution, the likelihood of the acquired aliased voxel for the N_c coils and the N_α excitations is:

$$P(a \mid X_A, \beta, \sigma^2) \propto (\sigma^2)^{-\frac{2N_cN_\alpha}{2}} \exp\left[-(a - X_A\beta)'(a - X_A\beta)/(2\sigma^2) \right]. \tag{9}$$

To separate the aliased images and estimate the voxel value for each slice, the least square estimation method is used. The estimated separate voxel value, $\hat{\beta}$, can be calculated by:

$$\hat{\beta}_{MLE} = (X_A' X_A)^{-1} X_A' a. \tag{10}$$

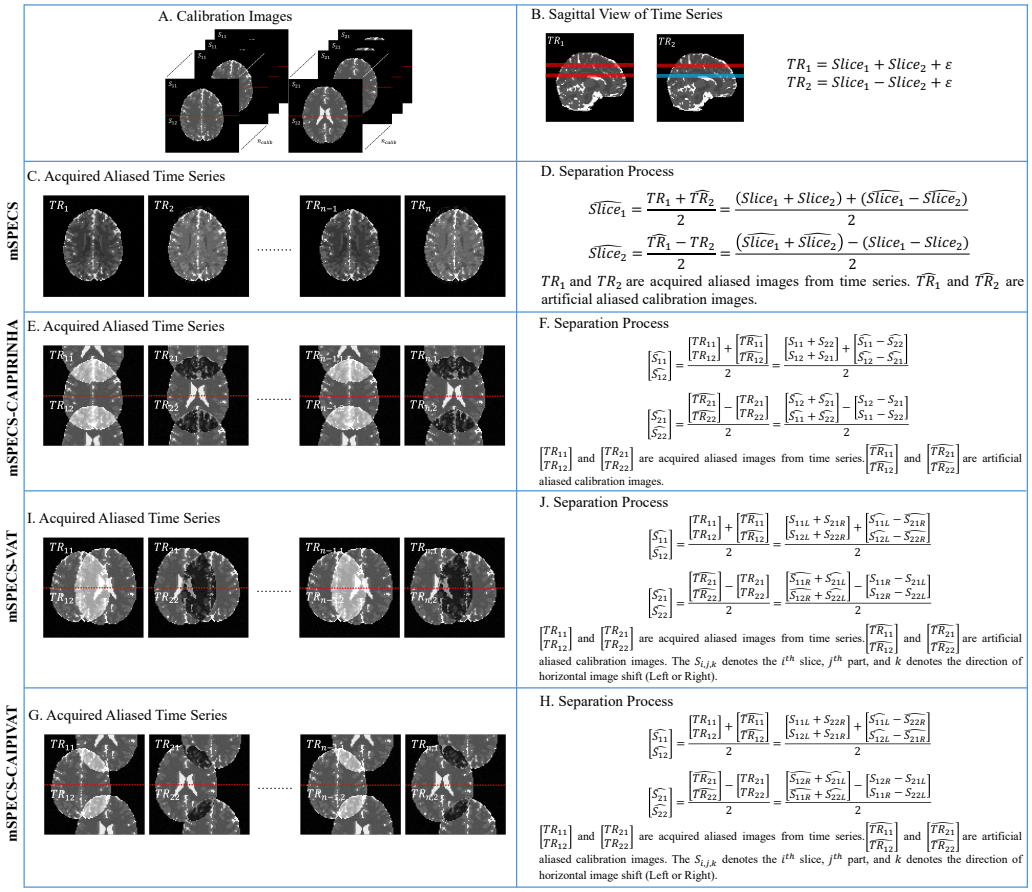

Figure 5: The data-acquiring process of the mSPECS technique (without any image shifts), the mSPECS-CAIPIRINHA technique (shift vertically), the mSPECS-VAT technique (shift horizontally), and the mSPECS-CAIPIVAT technique (shift vertically and horizontally).

Eq. 10 also can be used to calculate the reconstructed brain images in the SENSE model. In general, the determinant of X_A is close to zero, $\det(X_A) \approx 0$, which leads to failure in calculating the inverse of $X_A' X_A$. Thus, a bootstrap sampling method incorporated with artificial aliasing of reference calibration images technique are combined with the mSPECS-CAIPIVAT model. This combined technique can eliminate the inter-slice signal leakage artifacts by quantifying prior information in calibration images in a Bayesian model. More details is shown in the following section. Fig. 5 illustrates the data-acquiring process of the mSPECS technique (without any image shifts),

the mSPECS-CAIPIRINHA technique, the mSPECS-VAT technique and the mSPECS-CAIPIVAT technique.

2.2. The Bootstrap Sampling and Artificial Aliasing of Calibration Images

In the previous simultaneous multi-slice (SMS) study, bootstrap sampling and artificial aliasing of calibration reference image techniques have been proven as powerful tools to support the separation and reconstruction process of aliased images. By increasing the size of the aliasing matrix and adding a regularizer into the least square estimation function, the correlation induced by the separation process will decrease and the slice-to-slice signal leakage eliminated. In the fMRI time series, for each excitation, N_s bootstrap sampled coil slice images are randomly chosen from fully sampled calibration reference images. The mean calibration image is calculated for each slice and is artificially aliased, which is then repeated for each TR.

Given a single TR, the calibration images will have the same shift pattern as acquired images, thus, the total number of different combinations for different voxels should be N_s, which is equal to the rank of the chosen Hadamard matrix. After removing the combination of the acquired aliasing pattern from the full voxel combination pattern, N_s-1 different combinations remain. Therefore, for a single excitation, a voxel across N_s slices, measured through N_c coils, ν, can be represented as a vector with the dimension of $2N_sN_c(N_s-1)\times 1$ with the real component stacked on the top of the imaginary component, corresponding to the remaining combinations without the acquired aliasing combination. The mean bootstrap sampled voxel, $\bar{\nu}$, is the same dimension as ν for each time point. The artificial aliasing calibration images, ν, across N_s slices measured through N_c coils at N_α sequential time point can be expressed as:

$$\nu = C\bar{\nu} = C_A\mu + C\eta. \tag{11}$$

The dimension of the measurement error vector, η, is the same size as the vector ν. The mean of the measurement error for the calibration images is $E(\eta)=0$, and the covariance is $cov(C\eta)=\tau^2 I_{2N_cN_\alpha(N_s-1)}$, where $I_{2N_cN_\alpha(N_s-1)}$ is the identity matrix. It is assumed that there is no correlation between the real and imaginary components of the calibration images. The true voxel value vector, μ, is constructed with the real and imaginary components of the calibration voxel with the dimension $2N_s\times 1$. The artificial aliasing matrix, C_A, is following the same aliasing rules as acquired images do, rotating

by the matrix rotation operation and multiplying the Hadamard encoding aliasing coefficients. Due to the combination of acquired aliasing voxel removed from the full combinations, the dimension of the artificial aliasing matrix is $2N_cN_\alpha(N_s-1)\times 2N_s$. Same as the assumption in the acquired aliasing images, we assign $N_r=N_s$ to improve the computational efficiency. For example, considering a situation with $N_s=4$ and $N_r=4$, for each time point, $N_s-1=3$ combinations should be applied for the calibration images. Thus, for a given excitation, the δth Hadamard aliasing pattern and γth matrix rotating operation, the aliasing matrix $(C_A)_{\gamma,\delta}$ across N_c coils is:

$$(C_A)_{\gamma,\delta}=\left[\overline{H_{\delta,1}R_{\gamma,1}}\left(\ S_{1,1};\ldots;S_{N_c,1}\ \right),\ldots,\overline{H_{\delta,N_c}R_{\gamma,N_c}}\left(\ S_{1,N_s};\ldots;S_{N_c,N_s}\ \right)\right]. \tag{12}$$

The notation $\overline{HR}$ denotes the remaining combination for the Hadamard encoding aliasing pattern with the matrix rotation pattern after removing the combination of the acquired aliasing pattern. Incorporating N_α sequential time points, the artificial aliasing matrix, C_A, is:

$$C_A=\left[(C_A)_1,\ldots,(C_A)_{N_\alpha}\right]'. \tag{13}$$

Thus, the prior distribution of the artificial aliased calibration voxel is:

$$P(\nu\mid C_A,\mu,\tau^2)\propto(\tau^2)^{-\frac{2N_cN_\alpha(N_s-1)}{2}}\exp\left[-(\nu-C_A\mu)'(\nu-C_A\mu)/(2\tau^2)\right]. \tag{14}$$

The Eq. 6 and Eq. 11 can be combined together, which will generate:

$$y=\left[a;\nu\right]=\left[X_A\beta;C_A\mu\right]+\left[\varepsilon;C\eta\right]. \tag{15}$$

Based on the previous section, the covariance for the acquired aliasing measurement error is $cov(\varepsilon)=\sigma^2I_{2N_cN_\alpha}$, and the covariance for the artificial aliasing measurement error is $cov(C\eta)=\tau^2I_{2N_sN_c(N_s-1)}$, the covariance for vector, y, consisting of the acquired aliasing voxel value and the artificial aliasing voxel value is:

$$cov(y)=\begin{bmatrix}\sigma^2I_{2N_cN_\alpha} & 0\\ 0 & \tau^2I_{2N_cN_\alpha(N_s-1)}\end{bmatrix}. \tag{16}$$

Without the support of the bootstrapping technique, there is no variation in the artificial aliasing calibration images, i.e. the same calibration reference

images is artificially aliased for each TR, which will lead to $\tau^2 = 0$. However, by applying the bootstrapping technique, for each excitation, the N_s calibration images are randomly selected and averaged to obtain $\bar{\nu}$, and hence $\tau^2 = \sigma^2$. Thus, the covariance for vector, y, is:

$$cov(y) = \sigma^2 I_{2N_c N_\alpha N_s}. \tag{17}$$

2.3. The Prior Distribution

To estimate the reconstructed voxel value separated from the aliased slices, the voxels β are specified to have a normal prior distribution $\beta \sim N(\mu, \sigma^2(C_A^{'}C_A)^{-1})$, therefore:

$$P(\beta \mid \sigma^2, \mu, C_A) \propto (\sigma^2)^{-\frac{2N_s N_r}{2}} \exp\left[-(\beta-\mu)'(C_A^{'}C_A)(\beta-\mu)/(2\sigma^2)\right]. \tag{18}$$

The measurement error variance σ^2 is specified to have an inverse gamma prior distribution:

$$P(\sigma^2 \mid \lambda, \delta) \propto (\sigma^2)^{-(\lambda+1)} \exp\left[-\delta/\sigma^2\right], \tag{19}$$

where hyperparameters μ, λ and δ are assessed from the calibration images.

2.4. The Hyperparameters Assessment

Following the Bayesian process, the unknown hyperparameters can be assessed using the prior calibration images. In the image acquisition process of the mSPECS-CAIPIVAT model, two series of brain images from two different fMRI experiments are acquired: the calibration images and the aliased images. The aliased images correspond to the mSPECS-CAIPIVAT model, whereas the calibration images, on the other hand, are obtained using the traditional method without any image shift techniques or acceleration factors. Thus, the calibration images can be treated as prior information, and hyperparameters can be estimated from them. According to our Bayesian mSPECS-CAIPIVAT model, to estimate the voxel value β, we need to estimate the hyperparameters μ, λ, and δ. In Eq. 18, the artificial aliasing matrix C_A is known information and it strictly follows the artificial aliasing rules in Section. 2.2. The hyperparameter μ represents the averaged voxel value after the bootstrap resampling process, and its estimation is described in detail in Section 2.2. The hyperparameters λ and δ are the shape parameter and the scale parameter of the inverse-gamma distribution and we can assess them

from calibration images. As discussed in the Section. 2.2, for each excitation, N_s brain images will be randomly chosen from the fully sampled calibration images and averaged to assess hyperparameter μ. Moreover, the calibration reference images can be utilized to estimate sample noise variance σ_0^2. Therefore, the hyperparameters μ, λ and δ can be assessed by $\mu = \bar{\nu}$, $\lambda = n_0$ and $\delta = (n_0 - 1)\sigma_0^2$, where n_0 is the number of calibration images and σ_0^2 is sample noise variance.

2.5. The Posterior Estimation

Following Section. 2.3 and Section. 2.4, the joint posterior distribution for the voxel values β and the noise variance σ^2 can be obtained by combining the likelihood equation (Eq. 9), the prior distribution of β (Eq. 18) and the prior distribution of σ^2 (Eq. 19) together along with algebra to become:

$$P(\beta, \sigma^2 \mid \cdot) \propto \\ (\sigma^2)^{-\frac{p}{2}} \exp\left[-((\beta - \hat{\beta}_{MPM})'(X_A^{'} X_A + C_A^{'} C_A)(\beta - \hat{\beta}_{MPM}) + w)/(2\sigma^2)\right], \tag{20}$$

where $p = 2N_cN_\alpha + 2N_sN_r - 2\lambda - 2$, and $w = a^{'}a + \mu^{'}C_A^{'}C_A\mu - (X_A^{'}a + C_A^{'}C_A\mu)^{'}(X_A^{'}X_A + C_A^{'}C_A)^{-1}(X_A^{'}a + C_A^{'}C_A\mu) + 2\delta$. After integration, the marginal posterior distribution of estimate voxel value β is a student-t distribution $\beta \sim t(\nu^\star)$:

$$f(\beta \mid \cdot) \propto \left\{1 + \frac{1}{\nu^\star}(\beta - \hat{\beta}_{MPM})^{'}\left[\frac{(X_A^{'}X_A + C_A^{'}C_A)}{\tau^2}\right](\beta - \hat{\beta}_{MPM})\right\}^{\frac{\nu^\star+1}{2}}, \tag{21}$$

with $\nu^\star = p - 1$ and $\tau^2 = w/\nu^\star$. The marginal posterior mean (MPM) for $\hat{\beta}$ is:

$$E(\beta \mid \cdot) = \hat{\beta}_{MPM} = (X_A^{'}X_A + C_A^{'}C_A)^{-1}(X_A^{'}a + C_A^{'}C_A\mu). \tag{22}$$

The matrix $C_A^{'}C_A$ acts as a regularizer for the matrix inverse to improve the condition of the equation. Since the true voxel value from calibration images is close to the true voxel value from acquired aliased images, Eq. 22 leads to $E(\beta \mid \cdot) = \beta$. The marginal posterior covariance of the voxel value $\hat{\beta}$ is:

$$cov(\beta \mid \cdot) = \frac{\nu^\star}{\nu^\star - 2}\tau^2(X_A^{'}X_A + C_A^{'}C_A)^{-1}, \tag{23}$$

the separated voxel values are uncorrelated, meaning that there will not be signal leakage between slices. Moreover, the marginal posterior distribution

of σ^2 is an inverse gamma distribution, $\sigma^2 \sim IG(\gamma, w/2)$:

$$f(\sigma^2 \mid \cdot) \propto (\sigma^2)^{-\frac{p}{2}-1} \exp\left[-w/(2\sigma^2)\right], \tag{24}$$

with $\gamma = (p-1)/2$. The MPM of the noise variance σ^2 is:

$$E(\sigma^2 \mid \cdot) = \frac{w/2}{\gamma}, \tag{25}$$

and the marginal posterior variance of the noise variance is:

$$var(\sigma^2 \mid \cdot) = \frac{w/2}{(\gamma-1)^2(\gamma-2)}. \tag{26}$$

3. Simulation Study

3.1. Simulated FMRI Data

To investigate the performance of our proposed novel SMS technique, the mSPECS-VAT, the mSPECS-CAIPIRINHA and the mSPECS-CAIPIVAT model were applied to simulated fMRI data, and the results were compared with the mSPECS and the standard SENSE method. The simulated fMRI data has $TR = 510$ time points and mimics the real-world right hand finger tapping fMRI experiment. The first 20 time points will be omitted, thus leaving the simulated fMRI data with 490 time points. To replicate the full process of the real right-handed finger-tapping experiment, two time series were generated from the true noiseless axial view data: the calibration simulated data, and the task simulated data. The calibration simulated data includes $N_S = 8$ axial brain images without any simulated task activation blocks for each image. The task simulated data, in contrast, includes $N_S = 8$ axial brain images with simulated task activation blocks on the left motor cortex for the first 4 slices. No simulated activation blocks were added to the other 4 slices. The simulated activation blocks were added according to the in vivo experiment design, with the first 20 TRs off, following 15 TRs on and 15 TRs off for 16 epochs, and the last 10 TRs off. To achieve the $CNR = 0.5$, the mean magnitude of 0.04 was added to the simulated activation blocks for the first 4 slices. The mean magnitude of 4, to achieve $SNR = 50$, and different phase angles from 5° to 40° with 5° intervals were added to each image. In order to further increase the distinction of the spatial information for different tissue type, angle 7.5° was added to white matter (WM), 15° was added to

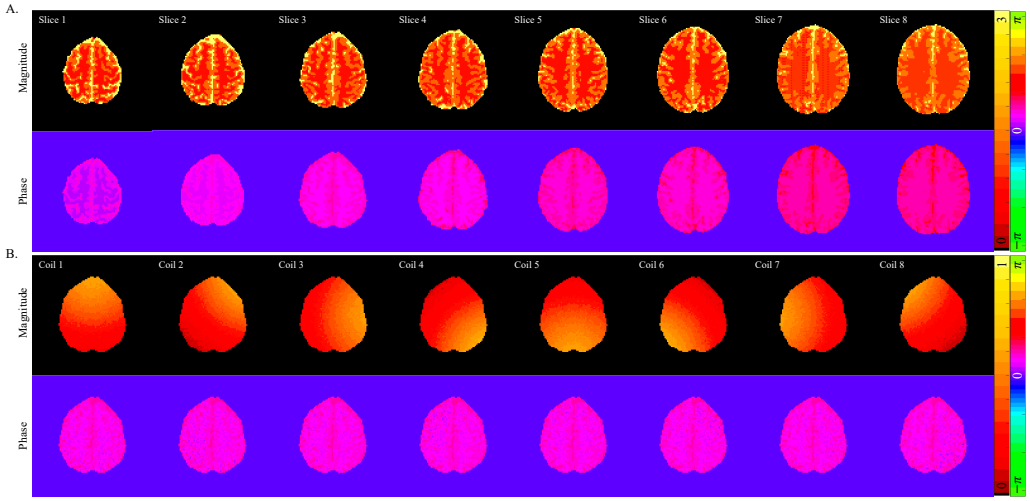

Figure 6: A. The true noiseless simulated magnitude and true phase information for axial brain images. B. The simulated magnitude and phase information of $N_C = 8$ channels coil for slice 3.

gray matter (GM), and 22.5° was added to the cerebral spinal fluid (CSF). Gaussian distribution noise $N(0, 0.0064)$ was added for each image of the calibration simulated data and the task simulated data separately. Fig. 6A shows the true noiseless simulated magnitude and true phase information for $N_S = 8$ axial brain images.

A total of $N_C = 8$ channel coil sensitivity profiles were simulated to weight each axial brain image. A mean magnitude of 0.95 and the different phase angles from 0° to 17.5° with 2.5° intervals were applied to each coil sensitivity. Fig. 6B shows the simulated magnitude and phase information of the $N_C = 8$ channel coil sensitivity profiles for the third axial brain image (slice 3). In the interest of investigating our new proposed SMS techniques under different TPA factors, we applied our model to three acceleration scenarios: TPA=2 (packet 1: slice 1 and 5, packet 2: slice 2 and 6, packet 3: slice 3 and 7, and packet 4: slice 4 and 8), TPA=4 (packet 1: slice 1, 3, 5 and 7, packet 2: slice 2, 4, 6 and 8), and TPA=8 (all slices into one packet). The number of packets multiplied by the acceleration factor equals the total number of images. All experiments were performed on MATLAB programming software.

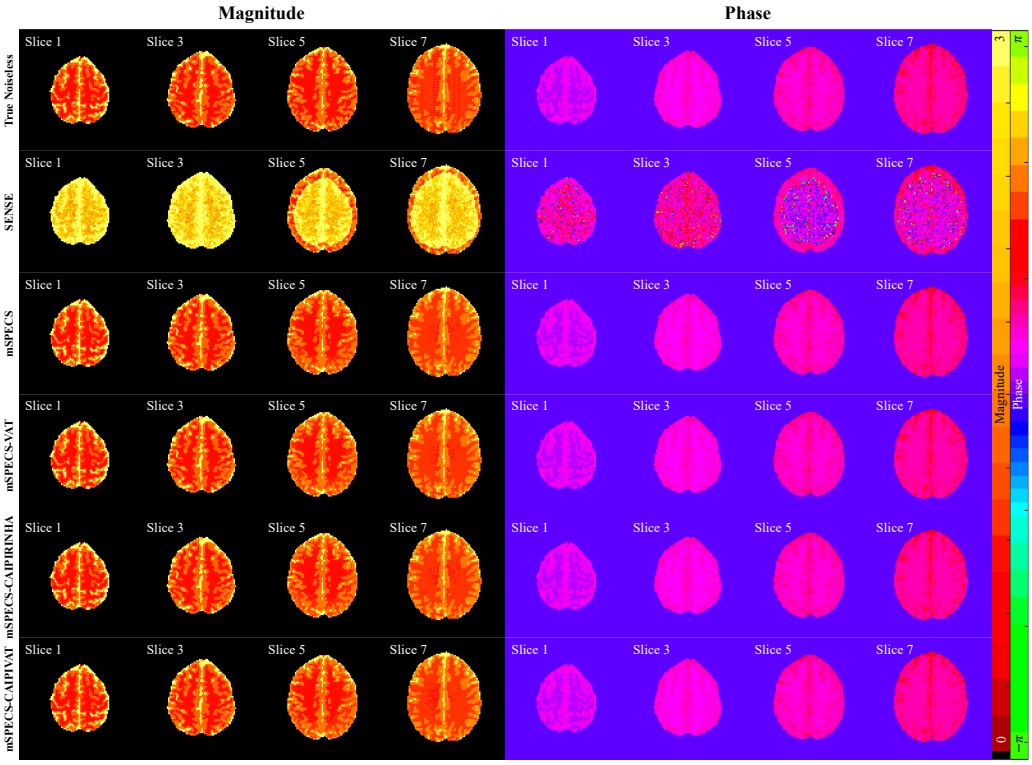

Figure 7: The true noiseless simulated magnitude and phase of the axial brain images compared with the temporal mean magnitude and temporal mean phase from SENSE, mSPECS, mSPECS-VAT, mSPECS-CAIPIRINHA and mSPECS-CAIPIVAT model for odd slices with TPA=2.

3.2. Non-Task Simulated Reconstruction Results

Following the methodology of the novel slice-wise image shift SMS technique, we conducted the simulated experiment using different through-plane acceleration factors: TPA=2, TPA=4, and TPA=8. We compared the reconstruction results under the same acceleration factors from the mSPECS model and the standard SENSE model. Fig. 7 shows the temporal mean magnitude and phase of the 490 time points reconstructed images from SENSE, mSPECS, mSPECS-VAT, mSPECS-CAIPIRINHA and mSPECS-CAIPIVAT model compared with the true magnitude and the phase of the brain images for odd slices with acceleration factor TPA=2. The temporal mean magnitude and phase were estimated according to Eq. 22. To avoid the error from averaging temporal mean phase at $(\pi, -\pi)$ boundary, the tem-

poral mean is calculated by $\bar{\phi} = angle(\sum \hat{\beta}_{MPM}/|\hat{\beta}_{MPM}|)$. The simulated reconstruction results for even slices of the four models can be found in Appendix A.1 Fig. A.14. As shown in Fig. 7, the mean magnitude and phase of the reconstructed images from the mSPECS, mSPECS-VAT, mSPECS-CAIPIRINHA, and mSPECS-CAIPIVAT models closely match the true values, indicating that these three models produce more accurate reconstructions. In contrast, the SENSE model yields the poorest reconstructions, with noticeable signal leakage from other aliased slices. As the acceleration factor increases to TPA=4 and TPA=8, the mSPECS, mSPECS-VAT, mSPECS-CAIPIRINHA, and mSPECS-CAIPIVAT models continue to provide reconstructions that closely resemble the true images. However, the reconstruction quality from the SENSE model significantly deteriorates, showing the worst performance.

The *SNR* value and g-factor value were also compared across four models. The temporal signal-to-noise ratio is defined as $SNR = \bar{S}/\sigma_N$, where $\bar{S}$ is the mean magnitude value in the time series, and σ_N is the standard deviation of the noise. The signal-to-noise ratio also can be expressed as $SNR = \beta_0/\sigma_N$, where β_0 is the baseline signal, and σ_N is the standard deviation of the magnitude of the noise. Based on the definition of *SNR* in Section 2.1.1, the g-factor can be calculated as $g_{accelerate} = \sqrt{N_s} SNR_{full}/SNR_{accelerate}\sqrt{R}$, where SNR_{full} is the *SNR* map from model without acceleration technique, and R indicates the in-plane acceleration factor, which in this case $R = 1$. The g-factor also indicates the noise amplification level of the model. Fig. 8 shows the temporal *SNR* map and g-factor map for the standard SENSE, mSPECS, mSPECS-VAT, mSPECS-CAIPIRINHA and mSPECS-CAIPIVAT models with through-plane acceleration factors TPA=2, TPA=4, and TPA=8 for slice 3. From Fig. 8, we observe that the standard SENSE model produces a low *SNR* map and a high g-factor penalty for all acceleration factors compared to the other four models. Increasing the through-plane acceleration factors reduces the *SNR* value and significantly increases the g-factor penalty. Although the mSPECS model offers a relatively good *SNR* map, the g-factor penalty increases as the through-plane acceleration factors rise. The mSPECS-VAT, mSPECS-CAIPIRINHA and mSPECS-CAIPIVAT models, however, provide better *SNR* and g-factor maps, with higher *SNR* values and lower g-factor penalties. As the through-plane acceleration factor increases, the *SNR* maps become brighter, indicating an increase in *SNR*, while the g-factor penalties remain relatively steady, as shown in Fig. 8.

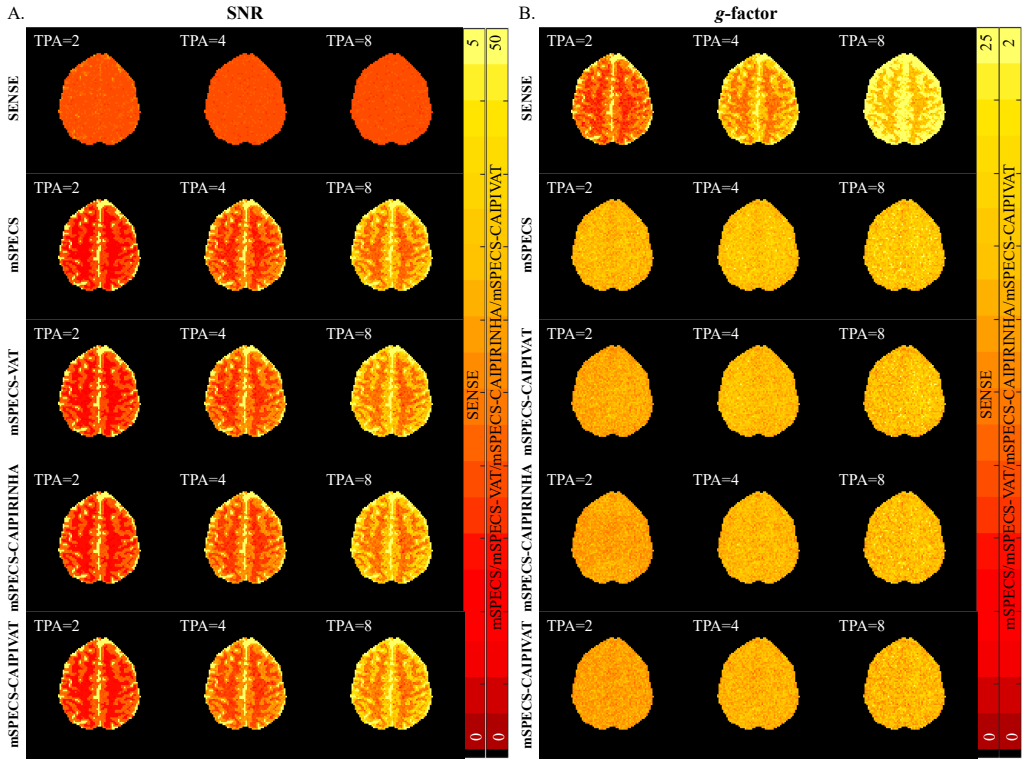

Figure 8: A. The *SNR* maps for SENSE, mSPECS, mSPECS-VAT, mSPECS-CAIPIRINHA and mSPECS-CAIPIVAT model with TPA=2, TPA=4, and TPA=8. The higher *SNR*, the better model performs. B. The g-factor maps for SENSE, mSPECS, mSPECS-VAT, mSPECS-CAIPIRINHA and mSPECS-CAIPIVAT model with TPA=2, TPA=4, and TPA=8. The closer g-factor is to 1, the better model performs.

3.3. Task Simulated Reconstruction Results

We also applied the novel slice-wise image shift SMS models to the simulated right-handed finger-tapping fMRI data with different through-plane acceleration factors TPA=2, TPA=4, and TPA=8, and compared the task activation results between each method. In the interest of further exploring the task detection ability for each model, two important criteria, the contrast-to-noise (*CNR*) value and the activation detection maps were also investigated. The *CNR* ratio is calculated as $CNR = \beta_1/\sigma_N$, where β_1 represents the task activation signal contrast. Activation detection was performed using a complex-valued model to compute fMRI activation ([25]). Fig. 9A shows the *CNR* map for SENSE, mSPECS, mSPECS-VAT, mSPECS-CAIPIRINHA

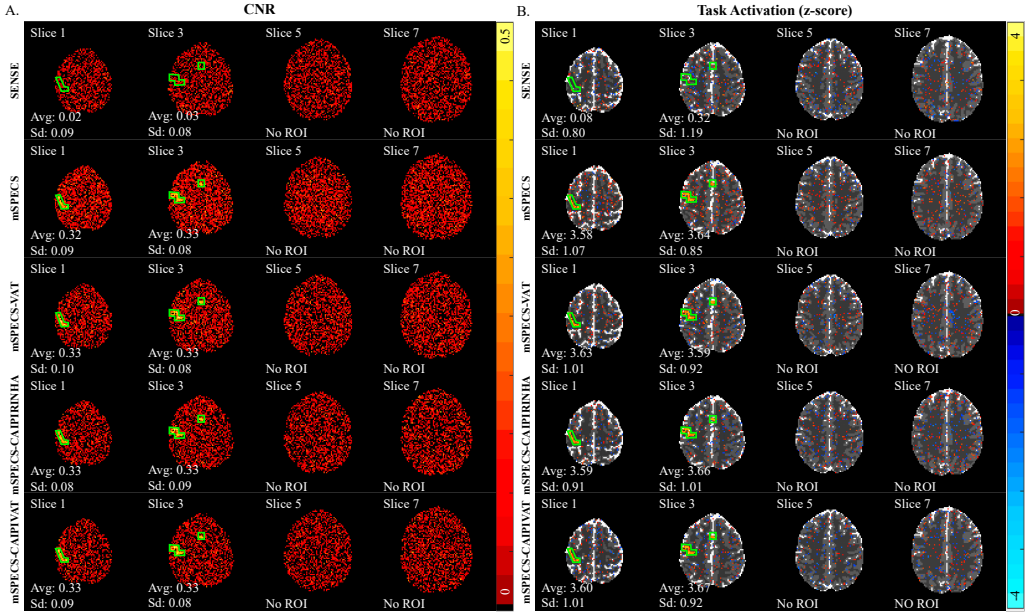

Figure 9: A. The *CNR* map and the average *CNR* value and standard deviation of *CNR* of ROI for SENSE, mSPECS, mSPECS-VAT, mSPECS-CAIPIRINHA and mSPECS-CAIPIVAT model for odd slices with TPA=2. B. The activation detection map and the average and standard deviation of z-score of ROI for SENSE, mSPECS, mSPECS-VAT, mSPECS-CAIPIRINHA and mSPECS-CAIPIVAT model for odd slices with TPA=2.

and mSPECS-CAIPIVAT model for odd slices at TPA=2, and the average *CNR* value and standard deviation of *CNR* value for region-of-interest (ROI). The *CNR* and the average *CNR* value and standard deviation of *CNR* value for region-of-interest (ROI) for four model of even slices can be found in Appendix A.2 Fig. A.21A. Since no simulated activation blocks were added to the last four slices, *CNR* values were not captured from those regions. In Fig. 9A, the SENSE model fails to capture any activation signal within the brain, while the mSPECS, mSPECS-VAT, mSPECS-CAIPIRINHA, and mSPECS-CAIPIVAT models successfully capture the simulated activation blocks with clear shapes and anatomical details. When comparing the average *CNR* value of the ROI, the mSEPCS-VAT, mSPECS-CAIPIRINHA and mSPECS-CAIPIVAT models demonstrate slightly higher values than the mSPECS model with TPA=2. To further examine the influence of the acceleration factor on activation detection, we compared the *CNR* maps of the four models at different acceleration factors. Fig. 10A displays the *CNR*

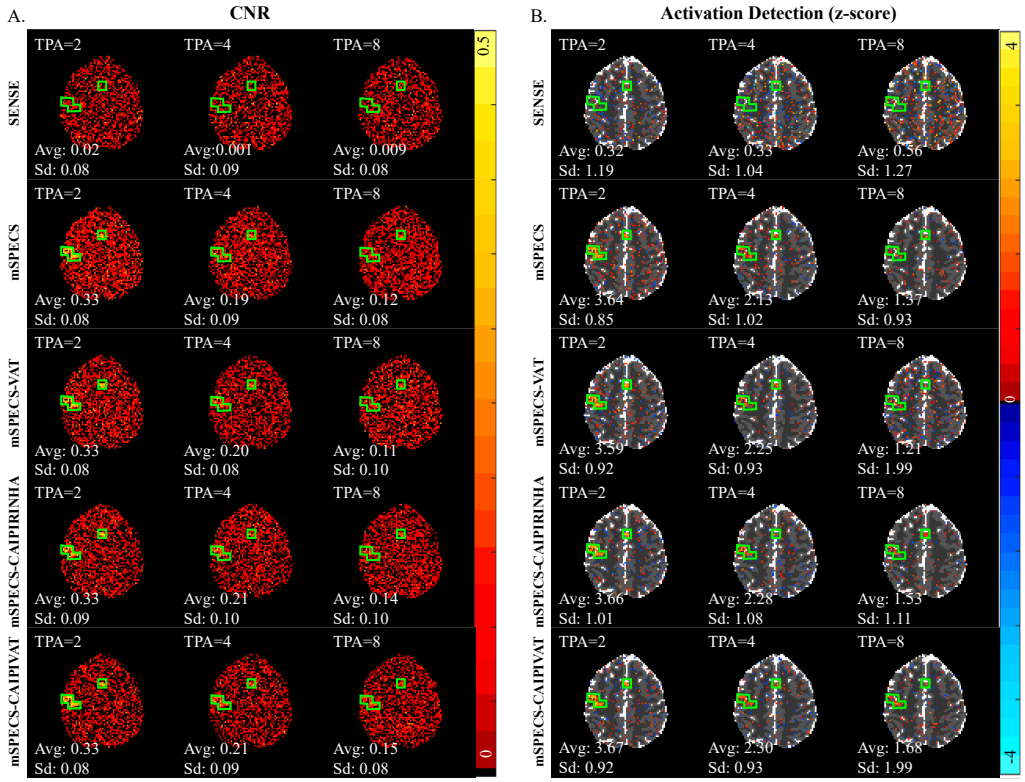

Figure 10: A. The *CNR* maps and average ROI *CNR* value from SENSE, mSPECS, mSPECS-VAT, mSPECS-CAIPIRINHA and mSPECS-CAIPIVAT model with respect to different acceleration factors TPA=2, TPA=4, and TPA=8 for slice 3. B. The task activation detection maps and average ROI z-score from SENSE, mSPECS, mSPECS-CAIPIRINHA and mSPECS-CAIPIVAT model with repect to acceleration factor TPA=2, TPA=4 and TPA=8 for slice 3. The higher *CNR* and z-score, the better model performs.

maps from the SENSE, mSPECS, mSPECS-VAT, mSPECS-CAIPIRINHA, and mSPECS-CAIPIVAT models for TPA=2, TPA=4, and TPA=8 in slice 3. As the acceleration factor increases, the average *CNR* value of the ROI decreases for the mSPECS, mSPECS-VAT, mSPECS-CAIPIRINHA, and mSPECS-CAIPIVAT models. However, the average *CNR* value in the three slice-wise image-shifting models remains slightly higher than in the mSPECS model. In contrast, the SENSE model fails to capture any simulated activation blocks at any acceleration factor. The mSPECS-CAIPIVAT provides the highest average *CNR* of the ROI among the three slice-wise image-shifting models with higher acceleration factors.

Concerning the main goal of this study is to improve the task activation detection rate, we also examined the activation detection map across four models. Fig. 9B shows the activation detection maps for odd slices from SENSE, mSPECS, mSPECS-VAT, mSPECS-CAIPIRINHA and mSPECS-CAIPIVAT model for odd slices at acceleration factor TPA=2. The activation detection maps for even slices from four models can be found in Appendix A.2 Fig. A.21B. Similar to the results observed in the *CNR* map, it is difficult to capture the simulated task activation blocks by applying the SENSE model. Additionally, the average z-score of the ROI from the SENSE model is the lowest among five models. In contrast, the mSPECS, mSPECS-VAT, mSPECS-CAIPIRINHA, and mSPECS-CAIPIVAT models can capture the simulated task activation blocks with complete shapes and anatomical structures. Comparing the average z-scores of the ROI from these three models, the three slice-wise image-shifting models, mSPECS-VAT, mSPECS-CAIPIRINHA and mSPECS-CAIPIVAT, exhibit higher significance levels than the mSPECS model. The mSPECS-CAIPIVAT model provides the highest average z-score of the ROI, indicating that it is more powerful in detecting activation signals than the other models. Similarly, we applied the four models with different acceleration factors to further investigate the activation detection process. Fig. 10B shows the task activation detection maps from the SENSE, mSPECS, mSPECS-VAT, mSPECS-CAIPIRINHA, and mSPECS-CAIPIVAT models at acceleration factors of TPA=2, TPA=4, and TPA=8 for slice 3. As the acceleration factor increases, the SENSE model fails to capture any task activation signals, and the average z-score of the ROI remains the lowest among the four models. The average z-score of the ROI from the mSPECS, mSPECS-VAT, mSPECS-CAIPIRINHA, and mSPECS-CAIPIVAT models decreases with increasing acceleration factor, and it becomes more challenging to capture the full shape of the task activation blocks. However, consistent with the *CNR* map results, the three slice-wise image-shifting models provide higher average z-scores of the ROI compared to the mSPECS model. The mSPECS-CAIPIVAT model offers the highest average z-score, confirming that it is more effective in detecting activation signals than the other models.

4. Experimental FMRI Study

4.1. Experimental FMRI Data

A 3.0 T General Electric Signa LX MRI scanner was used to perform a right-handed finger-tapping fMRI experiment on a single object. The experiment was designed with an initial 20s of rest, following 15s off and 15s on for 16 epochs, and a final 10s of rest. This results in a time series with 510 time repetitions was acquired for each repetition lasting 1s. The first 20s were disregarded leading to a time series with 490 time repetitions. An additional non-task time series was also acquired from the same object to serve as calibration time series. A flip angle of 90° with an acquisition bandwidth of 125kHz was applied in this experiment. The thickness of the axial brain slices was 2.5mm with 9 slices for each time repetition. Due to the nature of the Hadamard phase-encoding method, 8 slices were used to the new proposed reconstruction models and compared with the existing models. The most interior axial brain slice was disregarded. An 8 channel receiver coil was applied with dimension 96×96 for a 24 cm full FOV. The phase encoding direction is posterior to anterior. In order to acquire the 'true' reconstruction brain images and activation signals, the SENSE model was applied to each time repetition without any through-plane acceleration method, and the reconstructed images were treated as reference reconstruction images. Reconstruction results from SENSE, mSPECS, mSPECS-VAT, mSPECS-CAIPIRINHA, and mSPECS-CAIPIVAT model were compared to the reference reconstruction images.

4.2. Non-Task Experimental Reconstruction Results

In order to investigate the performance of the new slice-wise image shift SMS models on a real-world experiment, we applied mSPECS-VAT, mSPECS-CAIPIRINHA and mSPECS-CAIPIVAT model to the right-handed finger-tapping fMRI experiment time series. Reconstructed axial brain images were obtained from these three image shifting models and compared with the reconstruction results from SENSE and mSPECS models; reference images were also included in the comparison. We also investigated the model performance of the new slice-wise image shift models with different acceleration factors TPA=2, TPA=4 and TPA=8, and compared the reconstruction results with the SENSE and mSPECS model. Fig. 11 shows the temporal mean magnitude and mean phase of the reconstructed images from the reference, SENSE, mSPECS, mSPECS-VAT, mSPECS-CAIPIRINHA, and

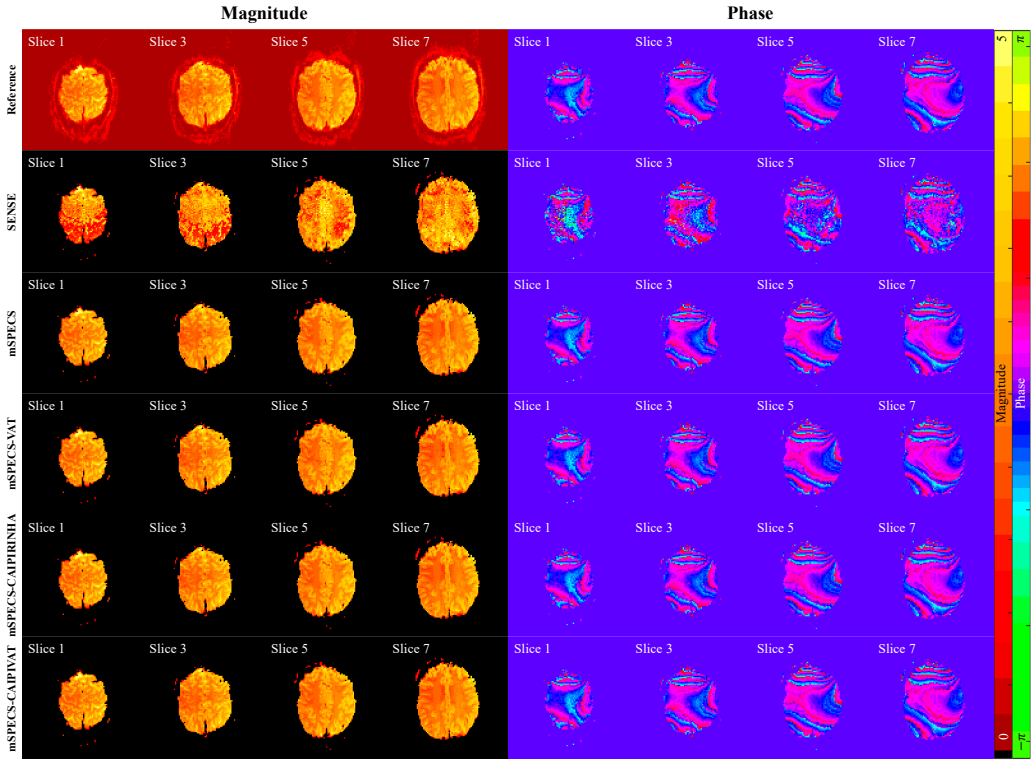

Figure 11: The temporal mean magnitude and temporal mean phase of the axial brain images from the reference, SENSE, mSPECS, mSPECS-VAT, mSPECS-CAIPIRINHA, and mSPECS-CAIPIVAT for odd slices with acceleration factor TPA=2.

mSPECS-CAIPIVAT model for odd slices with acceleration factor TPA=2. The temporal mean magnitude and mean phase for even slices of four models can be found in Appendix A.3 Fig. A.22. From Fig. 11, compared with the reference brain images, the reconstructed images from the SENSE model exhibit strong signal leakage from aliased slices, making anatomical structures difficult to discern. In contrast, the reconstructed images from the mSPECS, mSPECS-VAT, mSPECS-CAIPIRINHA, and mSPECS-CAIPIVAT models closely resemble the reference images, with clear anatomical structures.

Similar to the simulation reconstruction results, we also investigated the *SNR* and g-factor values of the reconstructed axial brain images of the four models. Fig. 12 shows the average and standard deviation of *SNR* and g-factor values of the ROI of reconstructed images for SENSE, mSPECS, mSPECS-VAT, mSPECS-CAIPIRINHA, and mSPECS-CAIPIVAT model

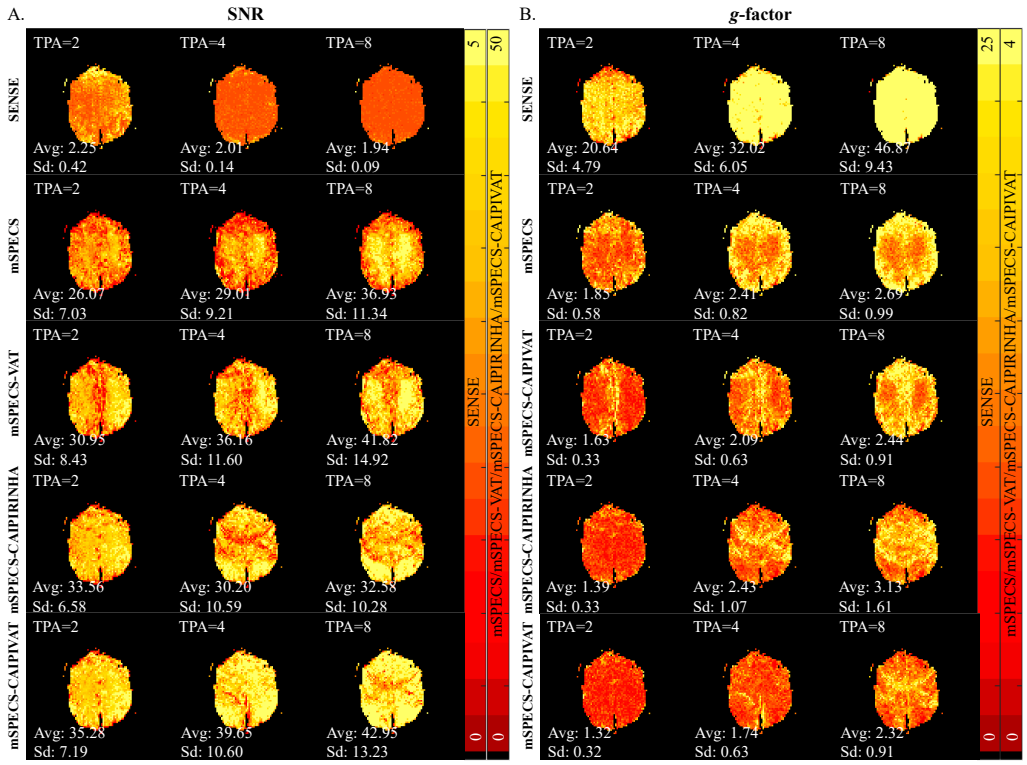

Figure 12: A. The *SNR* maps for SENSE, mSPECS, mSPECS-VAT, mSPECS-CAIPIRINHA and mSPECS-CAIPIVAT model with TPA=2, TPA=4, and TPA=8. B. The g-factor maps for SENSE, mSPECS, mSPECS-VAT, mSPECS-CAIPIRINHA and mSPECS-CAIPIVAT model with TPA=2, TPA=4, and TPA=8.

with different acceleration factors. From Fig. 12A, as the acceleration factor increases, the average *SNR* value of the ROI from the SENSE model decreases, whereas the average *SNR* values from the other three models increase. Comparing the mSPECS and the two slice-wise image shift techniques, the mSPECS-CAIPIVAT model provides the highest average *SNR* value of the ROI among these three models. From Fig. 12B, as the acceleration factor increases, the average g-factor value of the ROI from the SENSE model increases dramatically. On the other hand, similar to the results from the simulation reconstruction study, the average g-factor values of the ROI from the mSPECS, mSPECS-VAT, mSPECS-CAIPIRINHA, and mSPECS-CAIPIVAT models increase slightly, with the mSPECS-CAIPIVAT model providing the lowest average g-factor value among the four models.

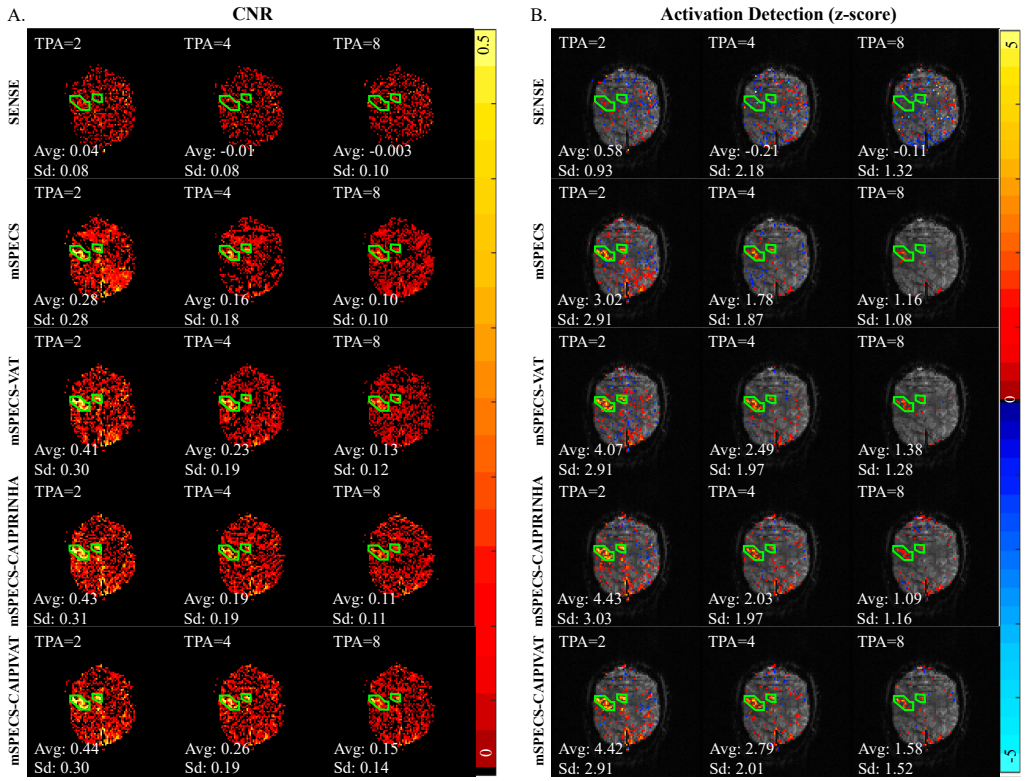

Figure 13: A. The *CNR* maps and average ROI *CNR* value from SENSE, mSPECS, mSPECS-VAT, mSPECS-CAIPIRINHA and mSPECS-CAIPIVAT model with respect to different acceleration factors TPA=2, TPA=4, and TPA=8 for slice 3. B. The task activation detection maps and the average ROI z-score from SENSE, mSPECS, mSPECS-VAT, mSPECS-CAIPIRINHA and mSPECS-CAIPIVAT model with respect to acceleration factor TPA=2, TPA=4 and TPA=8 for slice 3. The higher *CNR* and z-score, the better model performs.

4.3. Task Experimental Reconstruction Results

We also investigated the activation signal detection of the new proposed slice-wise image shift model by analyzing the *CNR* value map and the activation detection maps and comparing the reconstructed results with the SENSE and mSPECS model. We compared the average *CNR* value of the ROI between different models with different acceleration factors. Fig. 13A shows the *CNR* map for SENSE, mSPECS, mSPECS-VAT, mSPECS-CAIPIRINHA, and mSPECS-CAIPIVAT model with TPA=2, TPA=4, and TPA=8. As the acceleration factor increases, the SENSE model cannot capture any ac-

tivation signals. Furthermore, the average *CNR* value of the ROI decreases for the mSPECS, mSPECS-VAT, mSPECS-CAIPIRINHA, and mSPECS-CAIPIVAT models as the acceleration factor increases, indicating that as the number of aliasing slices increases, the activation blocks become harder to detect. However, the two slice-wise image-shifting techniques still provide higher average *CNR* values for the ROI than the mSPECS model, with the mSPECS-CAIPIVAT model providing the highest score. This means that the mSPECS-CAIPIVAT model is more powerful than the other three models in detecting activation blocks.

The activation detection maps were also investigated. Fig. 13B shows the activation detection map and the average z-score of the ROI from four models with different acceleration factors TPA=2, TPA=4, and TPA=8. The SENSE model cannot detect any activation blocks with any acceleration factor. Additionally, as the acceleration factor increases, the average z-score of the ROI decreases for the mSPECS, mSPECS-VAT, mSPECS-CAIPIRINHA, and mSPECS-CAIPIVAT models, indicating that detecting activation blocks becomes more challenging with more aliasing slices. However, when comparing the mSPECS model with the image-shifting techniques, the slice-wise image-shifting models provide higher average z-scores of the ROI, with the mSPECS-CAIPIVAT model having the highest average z-score. Thus, we reach the same conclusion as in the simulation study: the mSPECS-CAIPIVAT model is more powerful in detecting activation signals compared to the other models.

5. Discussion

Since fMRI studies were first introduced by [18], efforts have been made to enhance the efficiency of the signal acquisition procedure but still be able to achieve the goal of reconstructing brain images with high resolution, and improve the accuracy to capture the brain activation signal. Parallel imaging reconstruction methods, like SENSE, can be a potential solution to shorten the scan time with a through-plane subsampling technique. However, it is easily influenced by the high similarity of weighted coil sensitivity information of two aliased voxels, which leads to a singular matrix and a inter-slice signal leakage problem in the reconstruction process. In the interest of decreasing the similarity and increasing the independence of the weighted information of aliased voxels, slice-wise imaging shift techniques, CAIPIRINHA and CAIPIVAT, can increase the physical distance of the aliased voxels. Compared

to techniques without the image-shifting method, like SENSE and mSPECS, mSPECS-VAT, mSPECS-CAIPIRINHA and mSPECS-CAIPIVAT methods provide reconstructed images with more anatomic details and reduced temporal variance.

We also compared the average *SNR* values for different tissue types and the average g-factor values of these four models with respect to the different through-plane acceleration factors (Appendix A.1 Table A.1). Moreover, comparing the g-factor penalty among four models with respect to different acceleration factors, the mSPECS-CAIPIVAT model has the lowest value, which means that the mSPECS-CAIPIVAT model has a lower noise amplification level compared with other models. Thus, the image reconstruction method with slice-wise image shift techniques, mSPECS-VAT, mSPECS-CAIPIRINHA and mSPECS-CAIPIVAT, produce better results by increasing the *SNR* values and decreasing the variance of the reconstructed images. However, as shown in Fig. 10, increasing the through-plane acceleration factor leads to a loss in the average *CNR* values and the mean activation values of the task block when comparing the mSPECS, mSPECS-VAT, mSPECS-CAIPIRINHA, and mSPECS-CAIPIVAT models. With TPA increasing from 2 to 8, the mSPECS model shows a 63% decrease in *CNR* and a 62% decrease in mean activation. For the mSPECS-VAT model, *CNR* decreases by 66% and mean activation by 66%, the mSPECS-CAIPIRINHA model, *CNR* decreases by 63% and mean activation by 58%, while the mSPECS-CAIPIVAT model shows decreases of 54% for both *CNR* and mean activation. Thus, when comparing these four models, the SENSE model yields the worst results with strong inter-slice signal leakage. Compared to the mSPECS model, the slice-wise image shift SMS models have higher *SNR* and *CNR* values with lower g-factor penalty under the circumstance with high acceleration factors. Similar conclusions can be made from Fig. 13, compared with the mSPECS model, the slice-wise image shift techniques provide us higher *SNR* value for the ROI and lower g-factor penalty under the circumstance with high acceleration factor like TPA=8. However, we still need to face the situation where, with the high acceleration factor, the loss of the *CNR* value and the activation detection rate becomes significant. Therefore, by comparing the average *CNR* values for the ROI and activation detection maps among the four models, the mSPECS-CAIPIVAT model provides us the best *CNR* and activation detection map.

In this study, we discussed SMS models employing different slice-wise image shift techniques. Intuitively, the smaller the overlapping area between

aliased slices, the easier it is to separate them. Therefore, we compared the completely overlapping case, mSPECS model, with slice-wise image shift techniques, including mSPECS-VAT (horizontal), mSPECS-CAIPIRINHA (vertical), and mSPECS-CAIPIVAT (horizontal and vertical). Compared to slice-wise image shift techniques that operate in only one direction, as in mSPECS-VAT and mSPECS-CAIPIRINHA, the mSPECS-CAIPIVAT model utilizes shifts in both directions, resulting in a smaller overlapping area and consequently better reconstruction results. By comparing the results from the simulation reconstruction section and the experimental reconstruction section of the mSPECS-VAT, the mSPECS-CAIPIRINHA model and the mSPECS-CAIPIVAT model and to make a fair decision through a trade-off of the increment in the *SNR* and decrement of the *CNR* value and the activation detection with respect to different acceleration factors, we suggest the optimal through-plane acceleration factor to be TPA=4. Under this circumstance, the mSPECS-CAIPIVAT model can provide reconstructed images with high *SNR* information, but still be able to capture the activation signal. Our suggestion is consistent with the optimal multiband factor MB=4 from previous work ([23]).

6. Acknowledgments

The authors thank the Wehr Foundation as this research is funded by the Computational Sciences Summer Research Fellowship (CSSRF) at Marquette University in the Department of Mathematical and Statistical Sciences.

7. CRediT authorship contribution statement

Ke Xu: Writing– original draft, Visualization, Software, Investigation, Formal analysis. Daniel B. Rowe: Writing– review and editing, Supervision, Resources, Project administration, Methodology, Formal analysis, Conceptualization.

8. Declaration of competing interest

None declared.

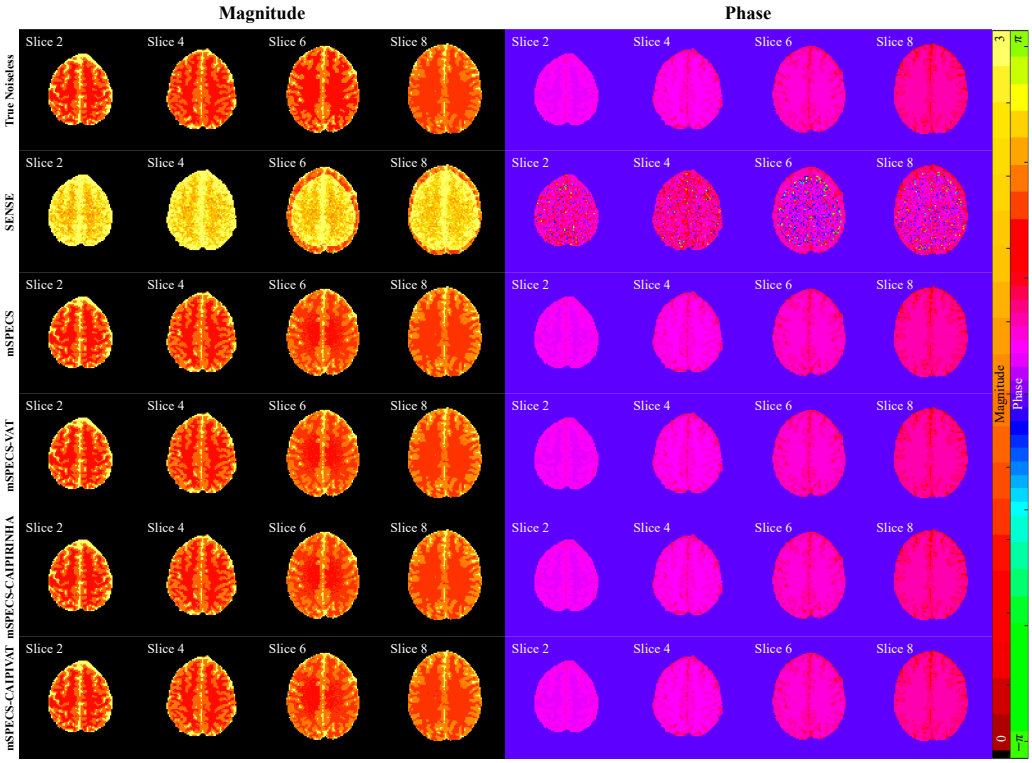

Figure A.14: The true noiseless simulated magnitude and phase of the axial brain images compared with the temporal mean magnitude and temporal mean phase from SENSE, mSPECS, mSPECS-VAT, mSPECS-CAIPIRINHA and mSPECS-CAIPIVAT model for even slices with TPA=2.

Appendix A. Supplement to Simulation Study and Experimental FMRI Study

Appendix A.1. Non-Task Simulated Reconstruction Results

In Section 3.2, we presented the temporal mean magnitude and temporal mean phase of the reconstructed axial brain images from odd slices using the SENSE, mSPECS, mSPECS-VAT, mSPECS-CAIPIRINHA, and mSPECS-CAIPIVAT models, and compared them with the true noiseless magnitude and phase. Fig. A.14 displays the temporal mean magnitude and temporal mean phase for the even slices of the reconstructed axial brain images with TPA=2. Significant signal leakage can be observed in the reconstructed images from the SENSE model, whereas the temporal mean magnitude and temporal mean phase from the mSPECS, mSPECS-VAT,

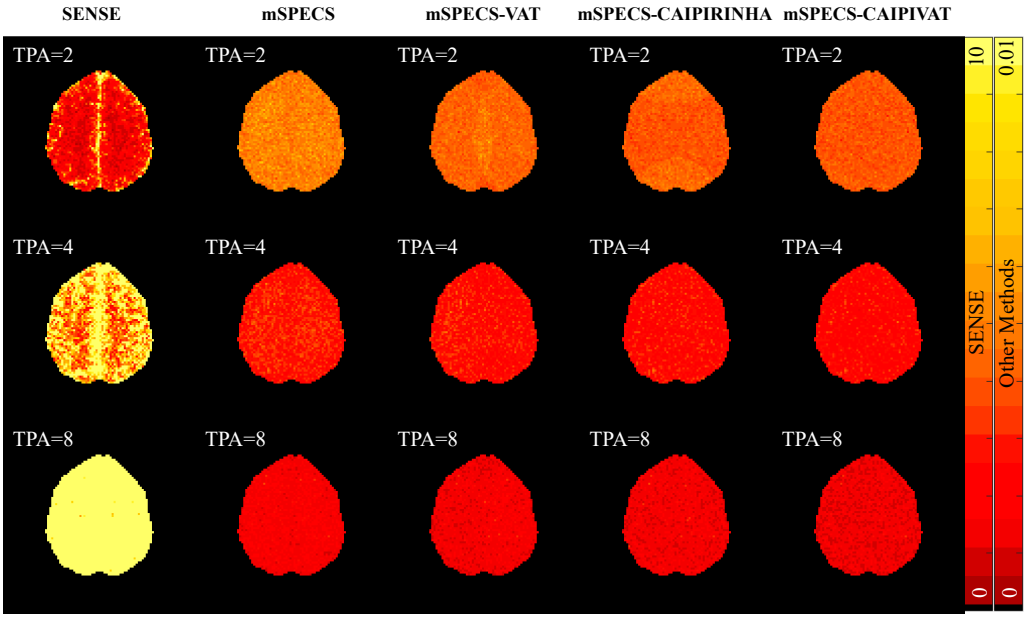

Figure A.15: The temporal variance of SENSE, mSPECS, mSPECS-VAT, mSPECS-CAIPIRINHA, and mSEPCS-CAIPIVAT model with different acceleration factors of slice 3.

mSPECS-CAIPIRINHA, and mSPECS-CAIPIVAT models closely match the true noiseless magnitude and phase.

To further analyze the performance of each model, Fig. A.15 illustrates the temporal variance of the reconstructed images from the SENSE, mSPECS, mSPECS-VAT, mSPECS-CAIPIRINHA, and mSPECS-CAIPIVAT models at different acceleration factors for slice 3. When comparing these four models, we observe a decreasing temporal variance from the SENSE model to the mSPECS-CAIPIVAT model at the same acceleration factor. As the acceleration factor increases, the temporal variance decreases for the mSPECS, mSPECS-VAT, mSPECS-CAIPIRINHA, and mSPECS-CAIPIVAT models, while it increases for the SENSE model. Among the three mSPECS-based models, the mSPECS-CAIPIVAT model achieves the lowest temporal variance.

Fig. A.16 shows the temporal mean of the variance of the reconstructed voxel value for slice 3 from SENSE, mSPECS, mSPECS-VAT, mSPECS-CAIPIRINHA, and the mSPECS-CAIPIVAT model with different acceleration factors. The variance of the reconstructed voxel value is calculated ac-

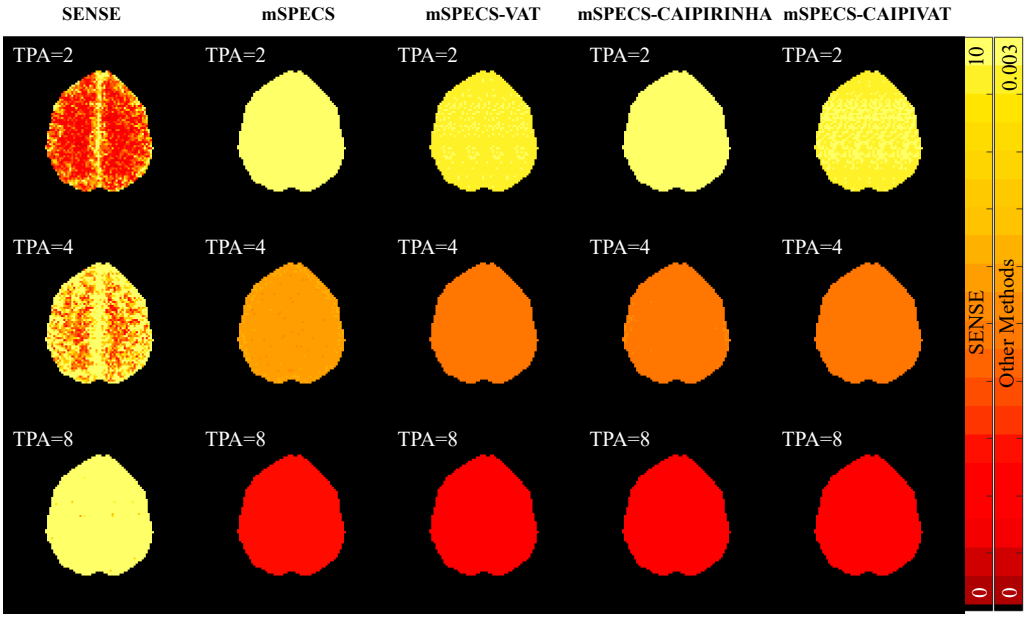

Figure A.16: The temporal mean of variance of the voxel value for slice 3 from SENSE, mSPECS, mSPECS-VAT, mSPECS-CAIPIRINHA, and the mSPECS-CAIPIVAT model with TPA=2, TPA=4, and TPA=8.

cording to Eq. 23. It also can be interpreted as the temporal mean of the variance of the baseline signal. In Fig. A.16, the SENSE model generates a higher temporal variance of the baseline signal compared to mSPECS, mSPECS-VAT, mSPECS-CAIPIRINHA, and the mSPECS-CAIPIVAT model for each acceleration factor. The temporal variance of the reconstructed voxel from the SENSE model increases as the acceleration factor increases, whereas the temporal variance of the reconstructed voxel from the other four models decreases with increasing acceleration factors. Compared to the mSPECS model, the models incorporating image shift techniques generate lower temporal variance, with mSPECS-CAIPIVAT exhibiting the lowest temporal variance of the baseline signal. Fig. A.17 shows the temporal mean of the residual variance from the SENSE, mSPECS, mSPECS-CAIPIRINHA, mSPECS-VAT, and mSPECS-CAIPIVAT model for slice 3 with TPA=2. The temporal mean of the residual variance is calculated according to Eq. 25. The results show a decreasing trend in the temporal mean of the residual variance from SENSE to mSPECS-CAIPIVAT, with the mSPECS-CAIPIVAT model yielding the lowest residual variance. Fig. A.18 shows the temporal

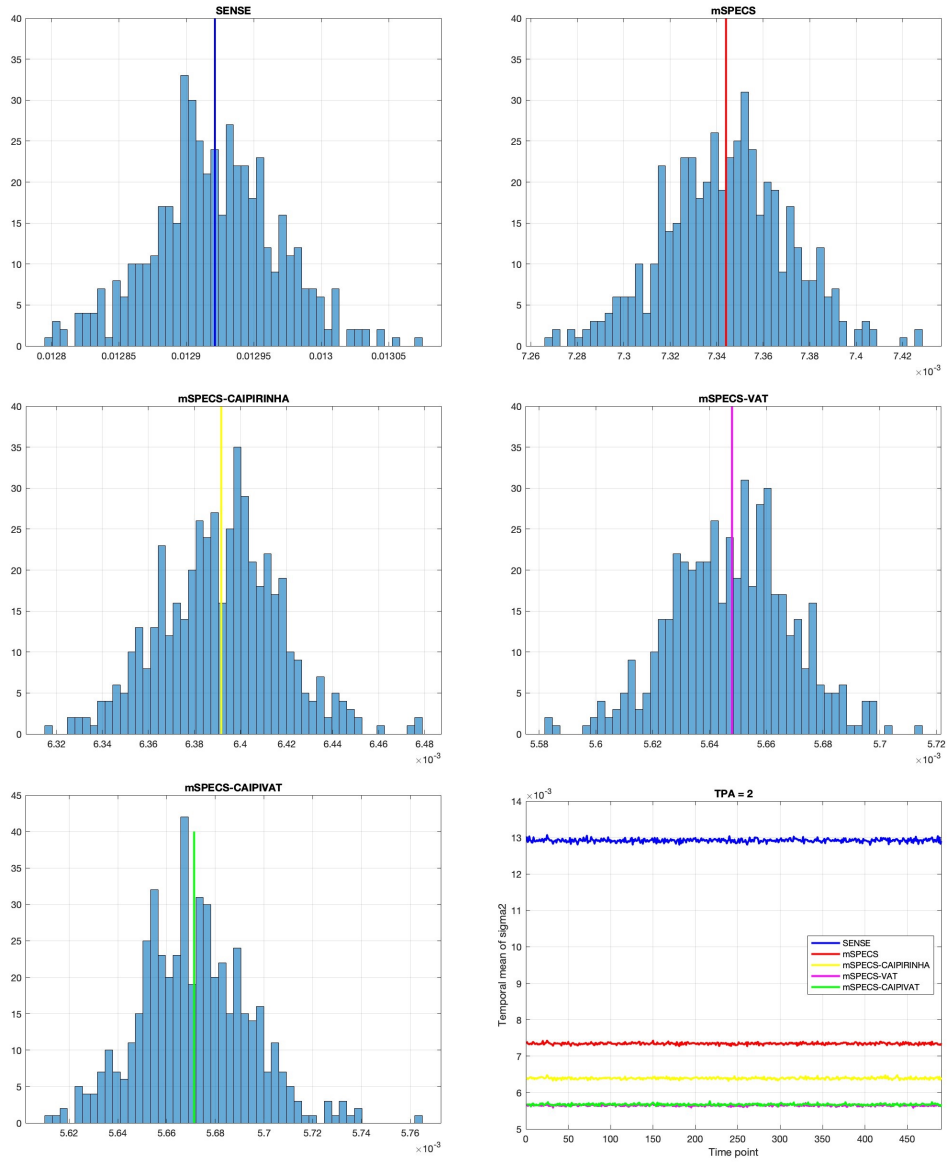

Figure A.17: The temporal mean of the residual variance for slice 3 from SENSE, mSPECS, mSPECS-CAIPIRINHA, mSPECS-VAT, and mSPECS-CAIPIVAT model with TPA=2.

mean of the residual variance for slice 3 from SENSE, mSPECS, mSPECS-CAIPIRINHA, mSPECS-VAT, and mSPECS-CAIPIVAT model with TPA=4 and TPA=8. From Fig. A.17 and Fig. A.18, as the acceleration factor in-

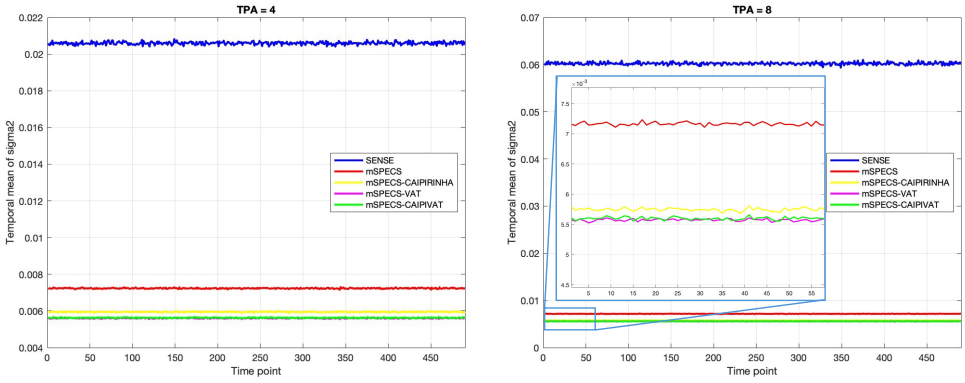

Figure A.18: The temporal mean of the residual variance for slice 3 from SENSE, mSPECS, mSPECS-CAIPIRINHA, mSPECS-VAT, and mSPECS-CAIPIVAT model with acceleration factor TPA=4 and TPA=8.

creases, the temporal mean of the residual variance increases for the SENSE model, whereas the other four models maintain a steady residual variance. For each acceleration factor, the mSPECS model exhibits a higher residual variance compared to models incorporating image shift techniques. Among these, the mSPECS-VAT and mSPECS-CAIPIVAT models yield the lowest temporal residual variance. Fig. A.19 shows the temporal variance of the residual variance of slice 3 from SENSE, mSPECS, mSPECS-CAIPIRINHA, mSPECS-VAT, and mSPECS-CAIPIVAT model with TPA=2. The temporal variance of the residual variance is calculated according to Eq. 26 in the main paper. Fig. A.20 shows the temporal variance of the residual variance of slice 3 from SENSE, mSPECS, mSPECS-CAIPIRINHA, mSPECS-VAT, and mSPECS-CAIPIVAT model with TPA=4 and TPA=8. From Fig. A.19 and Fig. A.20, the temporal variance of the residual variance for all models is close to zero. However, among these five models, the SENSE model produces the highest temporal variance. Compared to the models incorporating image shift techniques, the mSPECS model exhibits a higher temporal variance.

To evaluate and compare the changes in *SNR* and *g*-factor values for each tissue type across different methods and through-plane acceleration factors, Table A.1 presents the average *SNR* values for cerebral spinal fluid (CSF), gray matter (GM), and white matter (WM), as well as the average *g*-factor penalty for the whole brain. From Table A.1, we observe that the average *SNR* for CSF and GM in the standard SENSE model decreases

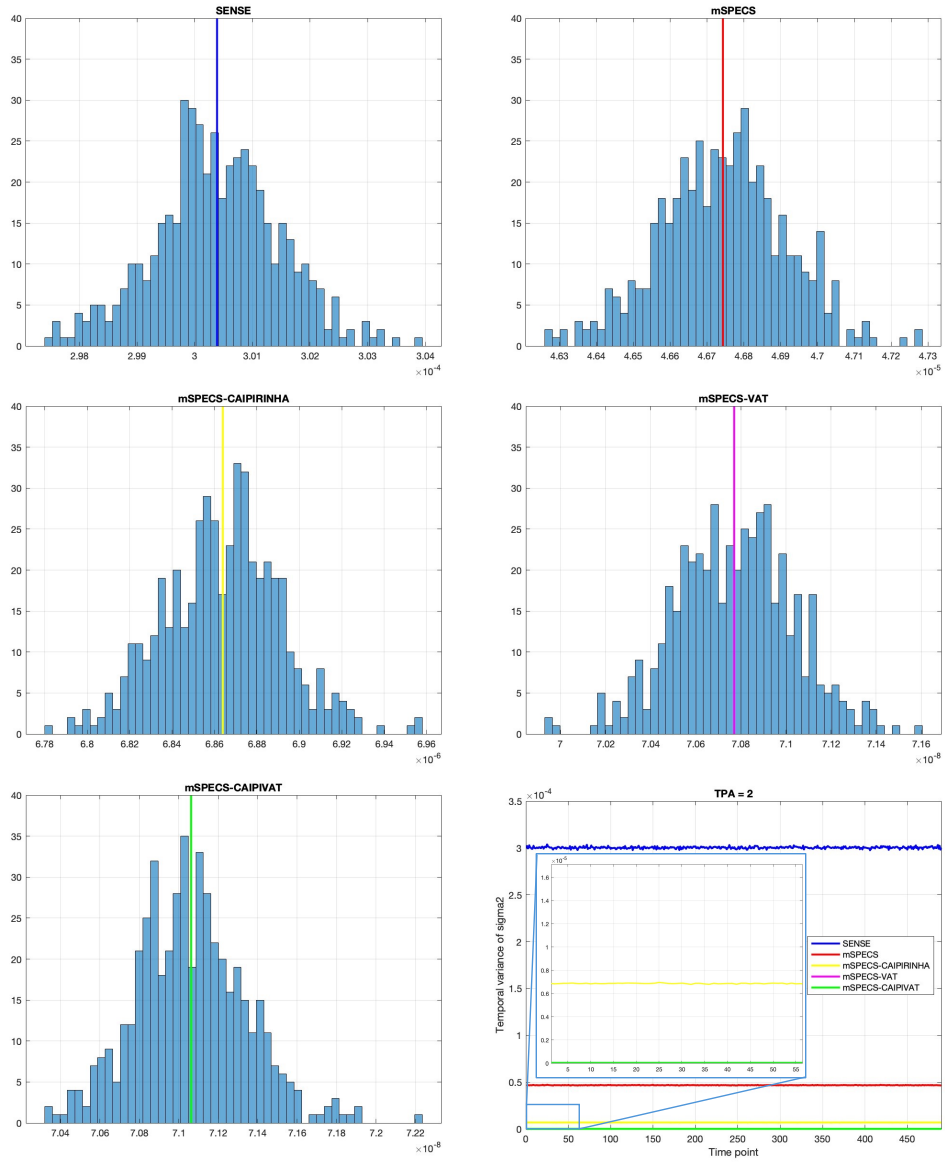

Figure A.19: The Temporal variance of the residual variance for slice 3 from SENSE, mSPECS, mSPECS-CAIPIRINHA, mSPECS-VAT, and mSPECS-CAIPIVAT model with TPA=2.

slightly as the through-plane acceleration factor increases, while the average *SNR* for WM remains unchanged. In contrast, the average *SNR* for all

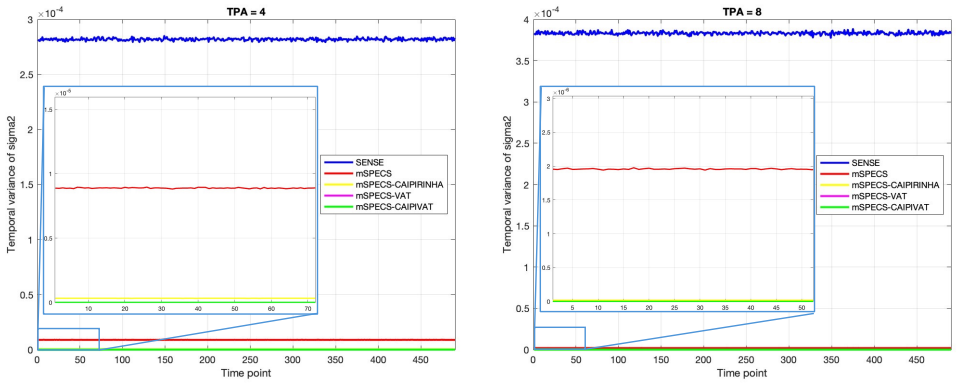

Figure A.20: The Temporal variance of the residual variance for slice 3 from SENSE, mSPECS, mSPECS-CAIPIRINHA, mSPECS-VAT, and mSPECS-CAIPIVAT model with TPA=4 and TPA=8.

tissue types in the other three models increases significantly with higher acceleration factors. Furthermore, the average g-factor for the SENSE model increases dramatically as the acceleration factor increases, compared to the modest increase in the average g-factor observed in the mSPECS, mSPECS-VAT, mSPECS-CAIPIRINHA, and mSPECS-CAIPIVAT models. Notably, compared to the mSPECS model, the three slice-wise image shift models, mSPECS-VAT, mSPECS-CAIPIRINHA and mSPECS-CAIPIVAT, exhibit lower average g-factor penalties, with the mSPECS-CAIPIVAT model showing the lowest average g-factor.

Appendix A.2. Task Simulated Reconstruction Results

In Section. 3.3, we presented the *CNR* map for the SENSE, mSPECS, mSPECS-VAT, mSPECS-CAIPIRINHA, and mSPECS-CAIPIVAT models for odd slices at TPA=2, along with the average *CNR* value and standard deviation for the region of interest (ROI). Fig. A.21 displays the *CNR* maps and task activation maps for even slices for the SENSE, mSPECS, mSPECS-VAT, mSPECS-CAIPIRINHA, and mSPECS-CAIPIVAT models with an acceleration factor of TPA=2. Similar to the conclusion drawn in the main paper, the *CNR* maps and task activation maps show that the SENSE model struggles to capture the activation signal in the left-hand side motor cortex within the brain images. In contrast, the other three models effectively capture the clear simulated activation blocks. Additionally, the slice-wise image shift techniques yield a higher average z-score for the ROI compared

Table A.1: The average *SNR* value for cerebrospinal fluid (CSF), gray matter (GM), and white matter (WM) with the average g-factor value of the whole brain with respect to SENSE, mSPECS, mSPECS-VAT, mSPECS-CAIPIRINHA, and mSPECS-CAIPIVAT methods with through-plane acceleration factors TPA=2, TPA=4, and TPA=8 for slice 3.

	SENSE			
Acceleration	CSF-*SNR*	GM-*SNR*	WM-*SNR*	g-factor
TPA=2	2.25	1.95	1.92	14.21
TPA=4	1.96	1.92	1.91	21.28
TPA=8	1.91	1.91	1.91	30.13
	mSPECS			
Acceleration	CSF-*SNR*	GM-*SNR*	WM-*SNR*	g-factor
TPA=2	55.00	19.06	12.11	1.30
TPA=4	73.49	25.29	16.11	1.39
TPA=8	101.14	34.92	22.20	1.44
	mSPECS-VAT			
Acceleration	CSF-*SNR*	GM-*SNR*	WM-*SNR*	g-factor
TPA=2	58.81	20.46	13.13	1.22
TPA=4	74.75	26.32	16.91	1.36
TPA=8	104.44	36.27	23.36	1.38
	mSPECS-CAIPIRINHA			
Acceleration	CSF-*SNR*	GM-*SNR*	WM-*SNR*	g-factor
TPA=2	59.85	21.13	13.54	1.16
TPA=4	76.25	26.87	17.38	1.27
TPA=8	104.98	36.82	23.69	1.34
	mSPECS-CAIPIVAT			
Acceleration	CSF-*SNR*	GM-*SNR*	WM-*SNR*	g-factor
TPA=2	61.11	21.41	13.73	1.15
TPA=4	78.19	27.56	17.89	1.27
TPA=8	107.72	37.97	24.50	1.29

to the mSPECS model. The mSPECS-CAIPIVAT model provides the highest average z-score for the ROI, indicating that it performs best in detecting activation signals.

Appendix A.3. Non-Task Experimental Reconstruction Results

In Section 4.2 of the main paper, we display the temporal mean magnitude and mean phase of the reconstructed images from the reference, SENSE, mSPECS, mSPECS-VAT, mSPECS-CAIPIRINHA, and mSPECS-CAIPIVAT models for odd slices with an acceleration factor of TPA=2. Figure A.22 presents the temporal mean magnitude and mean phase of the even slices of axial brain images from the reference, SENSE, mSPECS, mSPECS-VAT, mSPECS-CAIPIRINHA, and mSPECS-CAIPIVAT models with TPA=2. Aliased artifacts from other slices are clearly visible in the magnitude and phase reconstructed brain images from the SENSE model, whereas the mean magnitude and mean phase from the mSPECS, mSPECS-VAT, mSPECS-CAIPIRINHA, and mSPECS-CAIPIVAT models are closely aligned with the reference magnitude and phase. From Fig. A.23, we observe that the temporal variance from the SENSE model increases with increasing acceleration factor, whereas the temporal variance from the mSPECS,

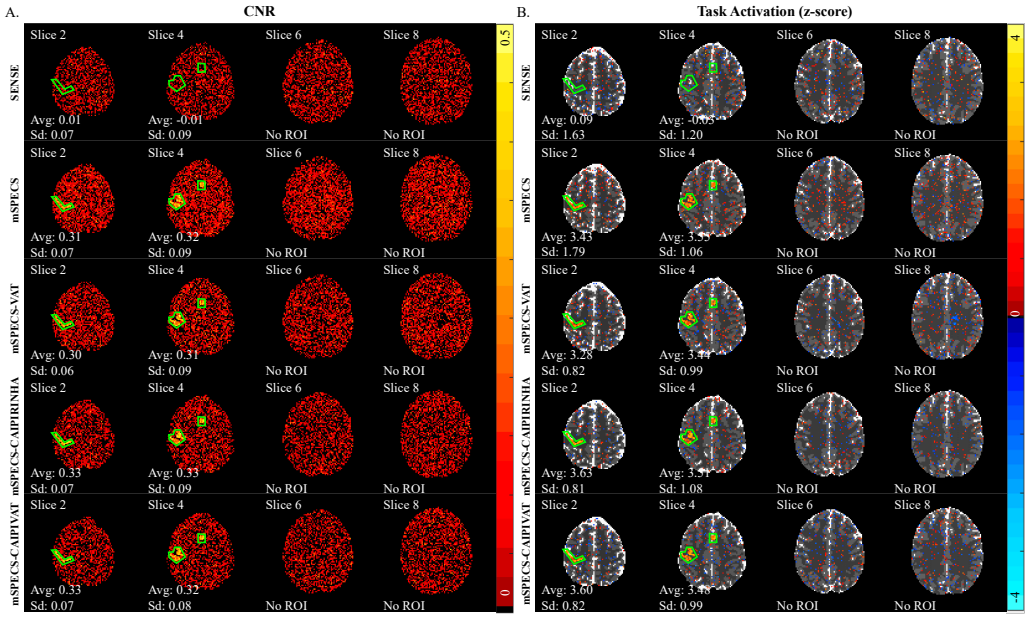

Figure A.21: A. The *CNR* map and the average *CNR* value and standard deviation of *CNR* of ROI for SENSE, mSPECS, mSPECS-VAT, mSPECS-CAIPIRINHA and mSPECS-CAIPIVAT model for even slices with TPA=2. B. The activation detection map and the average and standard deviation of z-score of ROI for SENSE, mSPECS, mSPECS-VAT, mSPECS-CAIPIRINHA and mSPECS-CAIPIVAT model for even slices with TPA=2.

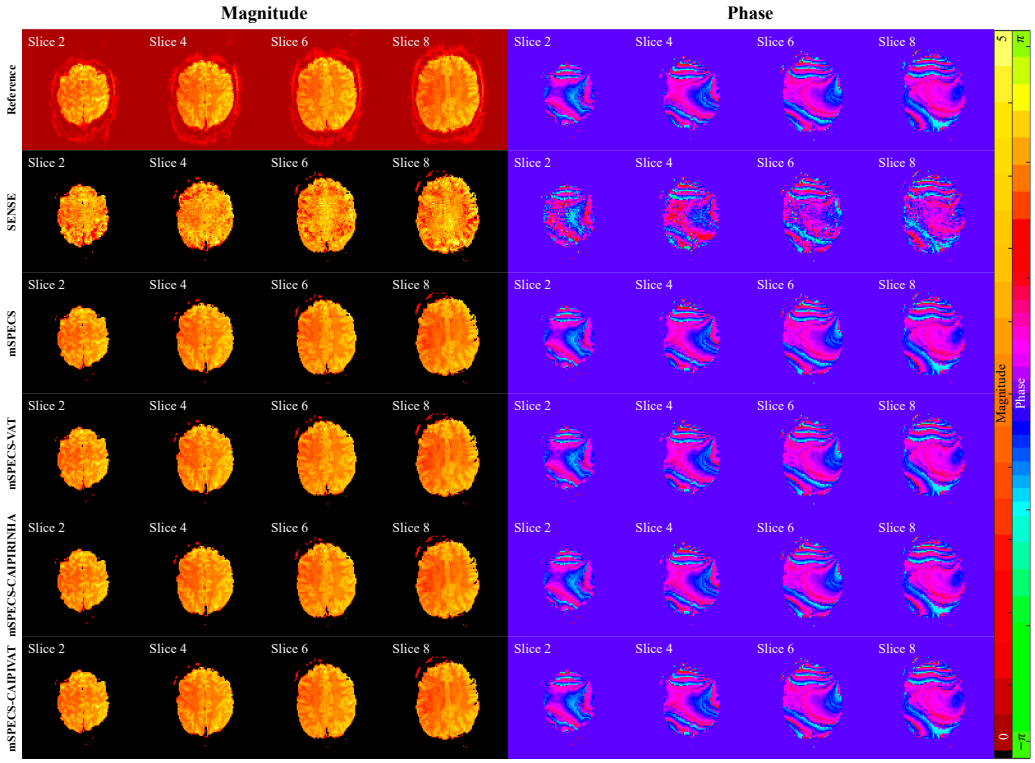

Figure A.22: The temporal mean magnitude and temporal mean phase of the axial brain images from the reference, SENSE, mSPECS, mSPECS-VAT, mSPECS-CAIPIRINHA, and mSPECS-CAIPIVAT for even slices with acceleration factor TPA=2.

mSPECS-VAT, mSPECS-CAIPIRINHA, and mSPECS-CAIPIVAT models decreases as the acceleration factor increases. Furthermore, when comparing the mSPECS model with the three slice-wise image shift techniques, the mSPECS-VAT, the mSPECS-CAIPIRINHA and mSPECS-CAIPIVAT models provide lower temporal variance, with the mSPECS-CAIPIVAT model yielding the lowest temporal variance results.

Appendix A.4. Task Experimental Reconstruction Results

Fig. A.24A shows the *CNR* value map for odd axial brain slices from the SENSE, mSPECS, mSPECS-VAT, mSPECS-CAIPIRINHA, and mSPECS-CAIPIVAT models with an acceleration factor of TPA=2. The average and standard deviation of the *CNR* values for the ROI are also shown in Fig. A.24A. From Fig. A.24A, it is evident that the SENSE model cannot

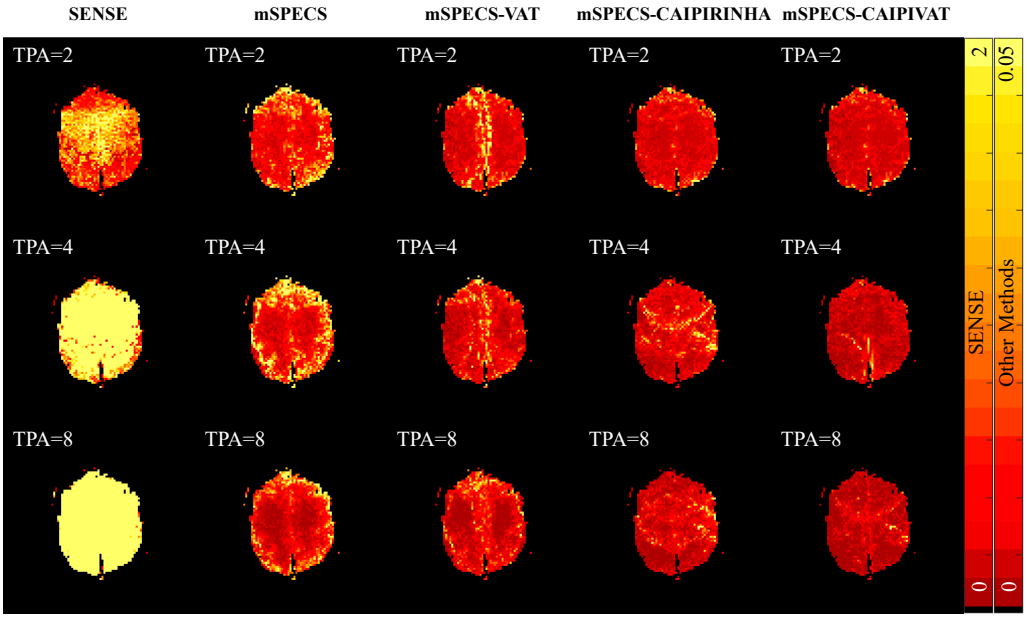

Figure A.23: The temporal variance of SENSE, mSPECS, mSPECS-VAT, mSPECS-CAIPIRINHA, and mSEPCS-CAIPIVAT model with different acceleration factors of slice 3.

detect any activation blocks in the right motor cortex brain area. In contrast, the other three models, mSPECS, mSPECS-VAT, mSPECS-CAIPIRINHA, and mSPECS-CAIPIVAT can detect clear activation blocks with detailed anatomical structures. When comparing the average *CNR* values of the ROI, the three slice-wise image shift techniques, mSPECS-VAT, mSPECS-CAIPIRINHA and mSPECS-CAIPIVAT, have higher values than mSPECS model. Fig. A.24B presents the activation block detection maps from the four models with an acceleration factor of TPA=2. The average and standard deviation of the z-scores for the ROI are also shown in Fig. A.24B. Similar to the *CNR* maps, the SENSE model fails to detect any activation blocks within the brain. The mSPECS, mSPECS-VAT, mSPECS-CAIPIRINHA, and mSPECS-CAIPIVAT models capture the activation signals with clear shapes and anatomical structures. The average z-score of the ROI from the two slice-wise image shift techniques is higher than that of the mSPECS model, with the mSPECS-CAIPIVAT model providing the highest average z-score for the ROI. A similar conclusion can be drawn from the *CNR* maps and task activation detection maps for even slices of the experimental recon-

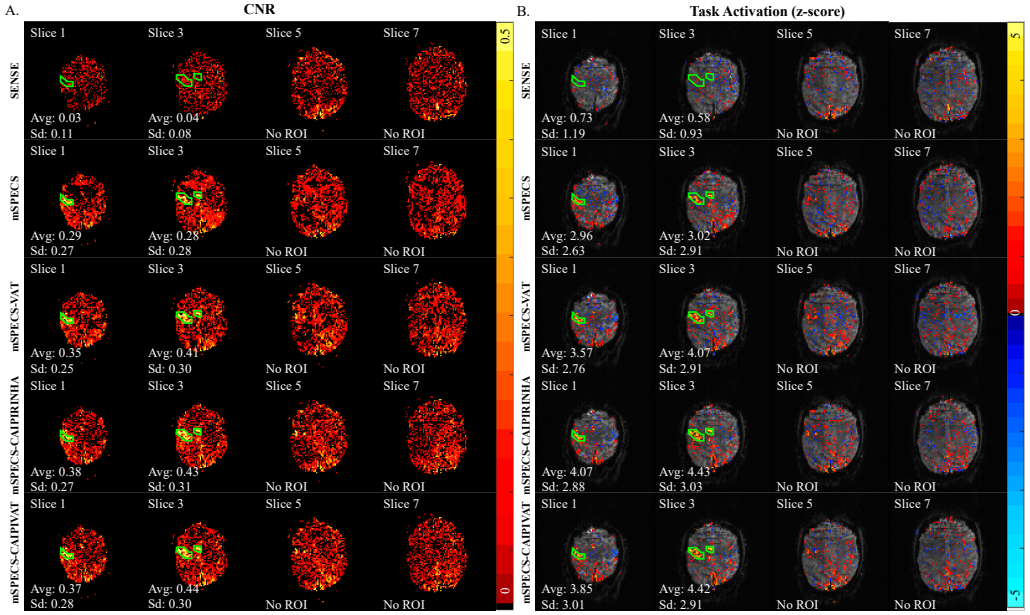

Figure A.24: A. The *CNR* map and the average *CNR* value and standard deviation of *CNR* of ROI for SENSE, mSPECS, mSPECS-CAIPIRINHA and mSPECS-CAIPIVAT model for odd slices with TPA=2. B. The activation detection map and the average and standard deviation of z-score of ROI for SENSE, mSPECS, mSPECS-CAIPIRINHA and mSPECS-CAIPIVAT model for odd slices with TPA=2.

structed images.

References

[1] Barth, M., Breuer, F., Koopmans, P. J., Norris, D. G., and Poser, B. A. *Simultaneous multislice (SMS) imaging techniques*, Magn Reson Med, 75(1):63–81. https://doi.org/10.1002/mrm.25897.

[2] Breuer, F. A., Blaimer, M., Heidemann, R. M., Mueller, M. F., Griswold, M. A., and Jakob, P. M. *Controlled aliasing in parallel imaging results in higher acceleration (CAIPIRINHA) for multi-slice imaging*, Magn Reson Med, 53(3):684–91. https://doi.org/10.1002/mrm.20401.

[3] Feinberg, D. A., Hale, J. D., Watts, J. C., Kaufman, L., and Mark, A. *Halving MR imaging time by conjugation: demonstration at 3.5 kG*, Radiology, 161(2), 527-531. https://doi.org/10.1148/radiology.161.2.3763926.

[4] Glover, G. H. *Overview of functional magnetic resonance imaging*, Neurosurg Clin N Am, 22(2):133–9, vii. https://doi.org/10.1016/j.nec.2010.11.001.

[5] Griswold, M. A., Jamob, P. M., Heidemann, R. M., Nikkka, M., Jellus, V., Wang, J., Kiefer, B., and Haase, A. *Generalized autocalibrating partially parallel acquisition (GRAPPA)*, Magn Reson Med, 47:1202–1210. https://doi.org/10.1002/mrm.10171.

[6] Hyde, J. S., Jesmanowicz, A., Froncisz, W., Kneeland, J. B., Grist, T. M., and Campagna, N. F. *Parallel image acquisition from noninteracting local coils*, Journal of Magnetic Resonance, 70(3), 512-517. https://doi.org/10.1016/0022-2364(86)90146-0.

[7] Jungmann, P. M., Ganter, C., Schaeffeler, C. J., Bauer, J. S., Baum, T., Meier, R., and Woertler, K. *View-Angle Tilting and Slice-Encoding Metal Artifact Correction for Artifact Reduction in MRI: Experimental Sequence Optimization for Orthopaedic Tumor Endoprostheses and Clinical Application*, PLoS One, 10(4):e0124922. https://doi.org/10.1371/journal.pone.0124922.

[8] Kim, M-O, Hong, T., and Kim, D-H. *Multislice CAIPIRINHA Using View Angle Tilting Technique (CAIPIVAT)*, Tomography, 43-48. https://doi.org/10.18383/j.tom.2016.00109.

[9] Kim, M-O, Zho, S-Y, and Kim, D-H. *3D imaging using magnetic resonanace tomosynthesis (MRT) technique*, Med. Phys, 39(8): 4733-4741. https://doi.org/10.1118/1.4737111.

[10] Kociuba, C. M. *A Fourier description of covariance, and separation of simultaneously encoded slices with in-plane acceleration in fMRI*, Ph.D. Dissertation, Marquette University, Milwaukee, Wisconsin, USA. https://epublications.marquette.edu/dissertations_mu/684/.

[11] Kornak J, Boylan R, Young K, Wolf A, Cobigo Y, Rosen H. *Bayesian Image Analysis in Fourier Space Using Data-Driven Priors (DD-BIFS)*, Information Processing and Management of Uncertainty in Knowledge-Based Systems, May 16;1239:380–90. https://doi.org/10.1007/978-3-030-50153-2_29.

[12] Kornak, J., Young, K., Schuff, N., Du, A., Maudsley, A. A., and Weiner, M. W. *K-Bayes reconstruction for perfusion MRI I: Concepts and application*, Journal of digital imaging, 23, 277-286. https://doi.org/10.1007/s10278-009-9183-y.

[13] Lindquist, M. A., Zhang, C. H., Glover, G., and Shepp, L. *Rapid three-dimensional functional magnetic resonance imaging of the initial negative BOLD response*, Journal of Magnetic Resonance, 191(1), 100-111. https://doi.org/10.1016/j.jmr.2007.12.016.

[14] Mansfield P. *Multi-planar image formation using NMR spin echoes[J]*, Journal of Physics C: Solid State Physics, 10(3): L55. 10.1088/0022-3719/10/3/004.

[15] Nencka, A. S., Shefchik, D. L., Huettner, A. M., and Jesmanowicz A. *Auto-Calibrated Multiband Imaging with Phase Tagging and Hadamard Encoding*, ISMRM Workshop on Data Sampling and Image Reconstruction, Sedona, AZ, 2013, 16. https://stan.jesmanowicz.com/andrzej/andre/refs/AJa_167.pdf.

[16] Nencka, A. S. and Jesmanowicz A. *Moving Window Auto-Calibrated Multiband Imaging for Minimized Residual Correlation*, ISMRM Workshop on Data Sampling and Image Reconstruction, Sedona, AZ, 2013, 11. https://stan.jesmanowicz.com/andrzej/andre/refs/AJa_161.pdf.

[17] Noll, D. C., Nishimura, D. G., and Macovski, A. *Detection in magnetic resonance imaging*, IEEE transactions on medical imaging, 10(2), 154-163. 10.1109/42.79473.

[18] Ogawa, S., Lee, T. M., Kay, A. R., and Tank, D. W. *Brain magnetic resonance imaging with contrast dependent on blood oxygenation*, Proc Natl Acad Sci USA, 87(24):9868-721. https://doi.org/10.1073/pnas.87.24.9868.

[19] Poustchi-Amin, M., Mirowitz, S. A., Brown, J. J., Mcinstry, R. C., and Li, T. *Principles and Applications of Echo-Planar Imaging: A Review for the General Radiologist*, RadioGraphics, 21:3, 767-779. https://doi.org/10.1148/radiographics.21.3.g01ma23767.

[20] Preibisch, C., Castrillón G., J. G., Bührer, M., and Riedl, V. *Evaluation of Multiband EPI Acquisitions for Resting State fMRI*, PLoS ONE, 10(9): e0136961. https://doi.org/10.1371/journal.pone.0136961.

[21] Pruessmann, K. P., Weiger, M., Scheidegger, M. B., and Boesiger, P. *SENSE: Sensitivity Encoding for Fast MRI*, Magn Reson Med, 42:952–962. https://doi.org/10.1002/(SICI)1522-2594(199911)42:5<952::AID-MRM16>3.0.CO;2-S.

[22] Rzedzian, R., Mansfield, P., Doyle, M., Guilfoyle, D., Chapman, B., Coupland, R. E., Chrispin, A., and Small, P. *Real-time nuclear magnetic resonance clinical imaging in pediatrics*, The Lancet, 322:1281-2. https://doi.org/10.1016/S0140-6736(83)91153-4.

[23] Risk, B. B., Murden, R. J., Wu, J., Nebel, M. B., Venkataraman, A., Zhang, Z., and Qiu, D. *Which multiband factor should you choose for your resting-state fMRI study?*, Neuroimage, 234:117965. https://doi.org/10.1016/j.neuroimage.2021.117965.

[24] Rowe, D. B., Bruce, I. P., Nencka, A. S., Hyde, J. S., and Kociuba, M. C. *Separation of parallel encoded complex-valued slices (SPECS) from a signal complex-valued aliased coil image*, Magn Reson Imaging, 34(3):359-69. https://doi.org/10.1016/j.mri.2015.11.003.

[25] Rowe, D. B., and Logan, B. R. *A complex way to compute fMRI activation*, Neuroimage, 23(3):1078-92. https://doi.org/10.1016/j.neuroimage.2004.06.042.

[26] Rowe, D. B., Nencka, A. S., Jesmanowicz, A., and Hyde, J. S. *Separation of two simultaneously encoded slices with a single coil*, In Proc Intl Soc Magn Reson Med, Vol. 21, p. 0123. https://ismrm.gitlab.io/2013/0123.html.

[27] Setsompop, K., Gagoski, B. A., Polimeni, J. R., Witzel, T., Wedeen, V. J., and Wald, L. L. *Blipped-controlled aliasing in parallel imaging (blipped-CAIPI) for simultaneous multi-slice EPI with reduced g-factor penalty*, Magn Reson Med, 67(5): 1210-1224. https://doi.org/10.1002/mrm.23097.

[28] Souza, S. P., Szumowskim, J., Dumoulin, C. L., Plewes, D. P., and Glover, G. *SIMA - simultaneous multislice acquisition of MR images by*

Hadamard-encoded excitation, J Comput Assist Tomogr, 12:1026–1030. https://pubmed.ncbi.nlm.nih.gov/3183105/.

[29] Welvaert, M. and Rosseel, Y. *On the Definition of Signal-To-Noise Ratio and Contrast-To-Noise Ratio for fMRI Data*, J PloS ONE, 8(11): e77089. https://doi.org/10.1371/journal.pone.0077089.